

Kymograph analysis with high temporal resolution reveals new features of neurofilament transport kinetics

J. Daniel Fenn¹  | Christopher M. Johnson² | Juan Peng³ | Peter Jung²  | Anthony Brown¹ 

¹Department of Neuroscience and Medical Scientist Training Program, Ohio State University, Columbus, Ohio 43210

²Quantitative Biology Institute and Department of Physics and Astronomy, Ohio University, Athens, Ohio 45701

³Center for Biostatistics and Department of Biomedical Informatics, Ohio State University, Columbus, Ohio 43210

Correspondence

Anthony Brown, Department of Neuroscience, Ohio State University, Rightmire Hall, 1060 Carmack Road, Columbus, OH 43210.

Email: brown.2302@osu.edu

Peter Jung, Department of Physics and Astronomy, Ohio University, Clippinger Hall, 139 University Terrace, Athens, OH 45701.

Email: jungp@ohio.edu

Funding information

NIH, Grant Numbers: R01 NS038526, S10 OD010383, P30 NS045758; NSF, Grant Numbers: IOS 1656784, IOS 1656785; Neuroscience Research Institute at The Ohio State University

Abstract

We have used kymograph analysis combined with edge detection and an automated computational algorithm to analyze the axonal transport kinetics of neurofilament polymers in cultured neurons at 30 ms temporal resolution. We generated 301 kymographs from 136 movies and analyzed 726 filaments ranging from 0.6 to 42 μm in length, representing $\sim 37,000$ distinct moving and pausing events. We found that the movement is even more intermittent than previously reported and that the filaments undergo frequent, often transient, reversals which suggest that they can engage simultaneously with both anterograde and retrograde motors. Average anterograde and retrograde bout velocities (0.9 and $1.2 \mu\text{m s}^{-1}$, respectively) were faster than previously reported, with maximum sustained bout velocities of up to 6.6 and $7.8 \mu\text{m s}^{-1}$, respectively. Average run lengths ($\sim 1.1 \mu\text{m}$) and run times (~ 1.4 s) were in the range reported for molecular motor processivity *in vitro*, suggesting that the runs could represent the individual processive bouts of the neurofilament motors. Notably, we found no decrease in run velocity, run length or run time with increasing filament length, which suggests that either the drag on the moving filaments is negligible or that longer filaments recruit more motors.

KEYWORDS

axon, axonal transport, kinetics, kymograph, neurofilament

1 | INTRODUCTION

Neurofilaments, which are the intermediate filaments of nerve cells, are space-filling cytoskeletal polymers that contribute to the expansion of axon cross-sectional area, thereby increasing axonal conduction velocity (Hoffman, 1995). In addition to this structural role, neurofilaments are also cargoes of axonal transport, distinct from membranous cargoes in that they are protein polymers, just 10 nm in diameter but many micrometers in length (Brown, 2003, 2014).

The axonal transport of neurofilament proteins was discovered in the 1970s using radioisotopic pulse-labeling studies in laboratory animals (Hoffman and Lasek 1975; Lasek, Garner, & Brady, 1984; Brown 2016). Radiolabeled neurofilament proteins synthesized in the neuronal cell bodies were found to be transported out along axons at average velocities of $0.1\text{--}2 \text{ mm day}^{-1}$, or approximately $0.001\text{--}0.02 \mu\text{m s}^{-1}$

(Lasek, Paggi, & Katz, 1993). More recently, time-lapse live-cell imaging of fluorescent neurofilament fusion proteins in cultured nerve cells has revealed that the proteins move in the form of assembled neurofilament polymers and that the movements are much faster than expected, but also infrequent and bidirectional (Roy et al., 2000; Uchida and Brown, 2004; Wang and Brown, 2001; Wang, Ho, Sun, Liem, & Brown, 2000; Yan and Brown, 2005; Yan, Jensen, & Brown, 2007). This apparent discrepancy between the pulse-labeling and live-imaging studies can be explained by the fact that neurofilaments spend most of their time not moving, leading to a slow average velocity (Brown, 2000). Thus, the slow velocity of neurofilament transport seen on long timescales is a temporal average of rapid movements interrupted by prolonged pauses: the movement is fast on a timescale of seconds but slow on a timescale of hours or days (Brown, Wang, & Jung, 2005; Craciun, Brown, & Friedman, 2005; Jung and Brown 2009; Li, Jung, & Brown, 2012).

We now know that the tracks for neurofilament movement are microtubules and that the movements are powered by microtubule motor proteins (Francis, Roy, Brady, & Black, 2005; Prahlad, Helfand, Langford, Vale, & Goldman, 2000; Shah, Flanagan, Janmey, & Leterrier, 2000). Though the movements are bidirectional, anterograde movements predominate. The retrograde movements appear to be driven by dynein and the anterograde movements appear to be driven by kinesin-1 (He et al., 2005; Helfand, Loomis, Yoon, & Goldman, 2003; Shah et al., 2000; Uchida, Alami, & Brown, 2009; Wagner et al., 2004). However, the relationship between these motors is poorly understood and many questions remain unresolved. For example, how and where do the motors interact with the neurofilaments, how many motors are recruited to move a single neurofilament, how do the motors interact to regulate neurofilament directionality and reversals, what determines the duration and frequency of the pauses, and how are the kinetics of neurofilament movement influenced by neurofilament length?

A major challenge in answering these questions is that neurofilaments are macromolecular assemblies well below the diffraction limit of light microscopes (Uchida, Monsma, Fenn, & Brown, 2016). To obtain sufficient signal and maximize the duration of our movies while minimizing photobleaching, we previously used relatively long exposures (1 s) and performed time-lapse imaging with long time intervals (4 or 5 s). While such studies provided us with considerable information regarding the kinetics of neurofilament transport at low temporal resolution, higher temporal resolution is required to explore questions about motor interaction and regulation. To address this, we have taken advantage of the improved speed and sensitivity of modern EMCCD cameras to image neurofilament movement at video rates using streaming acquisition. This faster frame rate has allowed us to perform kymograph analysis of neurofilament movement with >100-fold improvement in temporal resolution. To analyze these data, we used edge detection to define the trajectories of the filament ends and a novel computational filtering algorithm to automatically identify runs and pauses in the pixelated and noisy traces.

2 | METHODS

2.1 | Cell Culture and Transfection

Rat cortical neurons were cultured at low density with an astrocyte feeder layer using a modified version of the glial sandwich technique of Banker and colleagues (Kaech and Banker, 2006). Prior to plating, the dissociated cells were re-suspended in rat neuron Nucleofection reagent (VPG-1003) and transfected with a 2:1 mixture of pEGFP-NFM and pEB3-mCherry cDNA expression constructs by electroporation using an Amaxa Nucleofector (Lonza) set to program O-03. The pEGFP-NFM construct encoded an enhanced variant of green fluorescent protein (GFP) linked to the N-terminus of mouse neurofilament protein M (NFM) (Uchida et al., 2009), and the pEB3-mCherry construct encoded a red fluorescent protein (mCherry) fused to the N-terminus of human microtubule end-binding protein 3 (Efimov et al., 2008). After transfection, the cells were plated onto glass-bottomed culture dishes (assembled using No. 1.5 coverslips) and maintained in

NbActiv4™ medium (BrainBits). A more detailed description of these procedures is provided in Uchida et al. (2016).

2.2 | Live Imaging

Live imaging was performed on neurons in glass-bottomed culture dishes 7–10 days after plating using a Nikon TiE inverted wide-field epifluorescence microscope equipped with an Andor iXon Ultra 897 EMCCD camera (EM Gain = 200), a Lumencor SOLA LED light source, and a 100x/1.4NA Plan-Apochromat VC oil immersion objective. The microscope and camera were controlled using MetaMorph software (Molecular Devices). Prior to imaging, the NbActiv4™ medium was replaced with Hibernate-E medium (BrainBits, low fluorescence formulation), which buffers its pH at atmospheric CO₂. The temperature was maintained at 37°C using a Bioprotech objective heater and an Okolab H301-T stage-top incubator with humidity module.

We selected cells with low levels of GFP-NFM expression (evident by the absence of diffuse GFP fluorescence) and moved out along the axons until we encountered suitable gaps in the neurofilament array. To minimize photobleaching, we reduced the intensity of the exciting light from the LED light source to 2.5% of maximum power. To record neurofilament movement, we acquired 10,000 or 15,000 frames in “stream to RAM” acquisition mode using a Chroma ET-49002 GFP epifluorescence filter cube (Chroma Technology) and 30-ms exposures (total imaging time of 5 or 7.5 minutes, respectively). The camera read-out time was 0.3 ms, resulting in a time interval of 30.3 ms (33 frames per second).

After recording neurofilament movement, we recorded EB3-mCherry comets in the same field of view to confirm the orientation of the axon. For this purpose, we increased the intensity of the LED light source to 5% of maximum power and performed time-lapse imaging using an ET-49008 mCherry epifluorescence filter cube (Chroma Technology) with 200 ms exposures at 2 s time intervals for a total of 2–5 min.

2.3 | Image Processing

All image processing, including kymograph generation and edge detection and extraction, was performed in FIJI (Schindelin et al., 2012), a preconfigured variant of ImageJ (Schneider, Rasband, & Eliceiri, 2012).

2.4 | Kymograph Generation

To analyze neurofilament movement, we generated kymographs from time-lapse movies of GFP-tagged neurofilaments. We created maximum intensity projections of each movie stack to reveal the path of each filament, and thus the corresponding path of the axon. We then traced this path manually by drawing a multipoint line using the projected intensity as our guide, and then transferred this line onto the original stack. To generate a kymograph of the fluorescence intensity along this line, we used the FIJI plugin of Seitz & Surrey (2006) with a perpendicular line width of 5 pixels and a maximum intensity value sampling method. The intensity of each pixel in the resulting kymograph corresponded to the maximum fluorescence intensity extending across the width of the axon

at that location. Because sharp angles along the traced path can result in kymograph artifacts, we took care to increase the spatial sampling of the line in regions where the axon bends.

To determine the direction of neurofilament movement, we also generated kymographs from time-lapse movies of EB3-mCherry comets for each axon that we analyzed, as described above. To be confident in the assigned direction, we set a criterion that each axon must contain at least three visible comets, with at least 95% travelling in the same direction. Neurofilaments from axons that did not meet this criterion were excluded from our subsequent analysis.

2.5 | Edge Detection and Extraction

To automate the detection of filament ends in the neurofilament kymographs, we applied the Canny-Deriche edge-detection algorithm (Deriche 1987) as implemented in the "Edge Detection" third-party FIJI plugin (http://imagejdocu.tudor.lu/doku.php?id=plugin:edge_detection:start) originally authored by Thomas Boudier and then repackaged by Joris Meys. This algorithm includes a non-maximum suppression edge-thinning technique that sets pixels that are not part of local maxima to zero, creating dark channels around the detected edges. We used the default settings for all parameters except the α -value, which is an image smoothing parameter that determines the fidelity and continuity of the detected edges; low α values generate less sensitivity to local intensity gradients, resulting in more continuous edges at the expense of fidelity, whereas high α values generate greater fidelity to local intensity gradients, but also more irregular and less continuous edges, particularly in noisy images. Empirically, we selected $\alpha = 0.6$ as the best compromise for our images.

To extract the neurofilament edges, we overlaid an image of the detected edges in the Canny-Deriche output onto the original kymographs with 50% transparency in FIJI and then selected the desired edges manually in the overlay using the auto-wand region-of-interest tool. Any edges that were less than five time frames in length were ignored. Multiple edges or branches that extended less than 4 pixels from the primary edge were processed automatically as described in the pre-processing phase described below. Branches that extended 4 or more pixels away from the primary edge were deleted manually by erasing the pixel at the root of the branch, leaving only the primary edge selected for further analysis.

2.6 | Identification of Runs and Pauses

To identify runs and pauses in the filament trajectories extracted from these kymographs, we developed a custom pause-smoothing/run-filtering algorithm. The code for this algorithm was written in Fortran and can be made available upon request. The raw XY-coordinates for each edge were loaded into the algorithm and processed in four stages described below: pre-processing, pause-smoothing, run-filtering and post-processing.

2.6.1 | Pre-Processing

The neurofilament edges detected by the Canny-Deriche algorithm were rarely continuous for the entire movie, even for relatively bright

filaments, so for each filament edge in the kymograph traces we generally obtained multiple contiguous line segments separated by short temporal gaps. For the purpose of the subsequent data-filtering steps of our analysis, we temporarily filled these gaps by a linear interpolation to create a single, continuous edge for both ends of each filament. Importantly, this interpolation was temporary and these interpolated segments were flagged and subsequently removed before the final kinetic analysis. The longest gap encountered was 6,696 time frames, but 51% were four time frames or less. Occasionally, the algorithm identified multiple edges in a single time frame. In these instances, we averaged all edge locations for that time frame and then rounded the average to the nearest integer value to maintain the natural pixelation of the image. These pre-processing steps resulted in contiguous, one-pixel wide edges for both the proximal and distal ends of each filament.

2.6.2 | Pause-Smoothing

After pre-processing, the single continuous edges were subjected to an iterative noise-filtering step to smooth out pauses. In each iteration of the algorithm we sampled the location x of the filament edge at two time points t_i and t_j separated by an interval $\Delta t = t_j - t_i$, where $t_i < t_j$. If $x(t_i) \neq x(t_j)$ the time interval was considered to be a potential run and the pixels were left unmodified. Alternatively, if $x(t_i) = x(t_j)$ and if the location x of that filament edge during the time interval $[t_i, t_j]$ deviated by less than or equal to a specified noise threshold δ_{pixel} , the time interval was considered to be a potential pause and we set all positions of that filament end to the average position of the points in that time interval from t_i to t_j rounded to the nearest integer pixel value. If the edge deviated by greater than the noise threshold, we assumed that the interval $[t_i, t_j]$ was not a pause, and the pixels were left unchanged. Empirically the noise threshold was set at $\delta_{\text{pixel}} = \pm 2$ pixels for the present study.

The initial time window $\Delta t = [t_i, t_j]$ was equal to the duration of the entire trace. At each subsequent iteration, the window interval was reduced by one frame (i.e., one pixel in the time dimension of the kymograph) and the above filtering procedure was applied again. This continued until the smallest allowed window was reached, which was three time frames. To ensure sufficient sampling, each time window $[t_i, t_j]$ was sampled repeatedly at random locations along the filament trace until no more changes in the path occurred. Our final pause-smoothing criteria read as follows: for a randomly selected interval $[x(t_i), x(t_i + \Delta t)]$, if $x(t_i) = x(t_i + \Delta t)$ and $\max(\{X\}) - \min(\{X\}) \leq \delta_{\text{pixel}}$ where $\{X\} = \{x(t_i), x(t_i + \Delta t)\}$, then the time interval $[t_i, t_i + \Delta t]$ was defined as a pause having a pixel position $n_{\text{int}} (\langle x_j \rangle | x_j \in \{x(t_i), x(t_i + \Delta t)\})$.

2.6.3 | Run-Filtering

To define pausing and moving segments, we applied a run-filtering procedure to the pause-smoothed traces. First, we joined the corners of each pause segment in the stair-step traces of the pause-smoothed data with a straight line. This converted every pause segment in the trace into a sloped line with a corresponding velocity, i.e., a potential run, with shallower slopes for the pauses and steeper slopes for the runs (note that due to the interpolation resulting from this procedure, it

was possible for the analysis to generate half pixel, i.e., 0.08 μm , run lengths). We then applied an empirically determined pause cut-off (see Results) to define what constitutes a “running” event versus a “pausing” event. All segments of the filament traces that had a velocity equal to or above the cut-off were defined as runs and retained their run-filtered slope value as the assigned velocity for that segment, whereas all segments with velocities below the cut-off were defined as pauses and were reverted back to their pause-smoothed position with a corresponding velocity of zero.

2.6.4 | Pause Blocks and Run Blocks

The above thresholding procedure for identifying runs and pauses occasionally generated contiguous adjoining pause segments with different positional values, or contiguous adjoining run segments with different velocities, that is, pause segments that had no intervening run, with an apparent instantaneous change in position at their junction, or run segments that had no intervening pause, with an apparent instantaneous change in velocity at their junction. To address this, we combined contiguous adjoining pause segments or run segments into larger “pause blocks” or “run blocks,” respectively. In other words, for the purposes of our subsequent kinetic analysis, we considered contiguous pause segments to be a single pause, and contiguous run segments to be a single run. The velocities of the run blocks were calculated as a time-weighted average of the velocities of the individual run segments.

2.6.5 | Post-Processing

The above procedure resulted in separate traces for the proximal and distal ends of the filaments, each segmented into moving and pausing events. We then removed all portions of these traces that were flagged as part of the temporary gap filling that occurred in the pre-processing step. This procedure resulted in the truncation of some pauses or runs. Because the gaps arose from edge detection issues unrelated to the kinetics of neurofilament movement, inclusion of these truncated runs and pauses would lead us to underestimate the actual duration of those events. Thus, we excluded from our analysis all runs that were not flanked by pauses, or by runs in the opposite direction, and all pauses that were not flanked by runs. In total, for the present study, these data exclusion steps resulted in loss of $\sim 35\%$ of the data, reducing the number of analyzable time points from 8,639,333 to 5,572,121.

2.7 | Data Handling and Processing

The Fortran code that we created to run the above algorithm steps generated detailed numerical output in the form of text files, including pause kinetics (pause time, start frame and end frame for each pause block), run kinetics (length, time, velocity, directionality, start frame and end frame for each run block), and X-Y coordinates for the filaments at each stage of the algorithm (raw, pause-smoothed, run-filtered, and final output data). These data were then combined for our population-based analysis. Importantly, no weighting was assigned to any filament or segment and each run and pause was considered an independent event. Data visualization and histogram binning were performed using Matlab or the Matplotlib 2.0 package within Python 2.7.

2.8 | Statistical Analysis

The relationship between filament length and various kinetic parameters and states of neurofilament movement were tested using mixed-effects modeling. Random effects included a filament-specific random intercept, accounting for within-filament correlation, and a random effect for animal (i.e., culture batch), accounting for nested data from the same animal. A Kenward–Roger adjustment to the degrees of freedom was used to control Type I error rates. For the tests of differences in filament length between the kinetic states (pausing, moving antero-grad, moving retrograde), the filament lengths were natural-log-transformed to better approximate normality of the residuals. Tukey’s method was used for multiple comparisons. For the tests of differences in the kinetic parameters of neurofilament movement with respect to filament length, the kinetic parameters (run velocity, run length, run time, pause time) were also natural-log-transformed to better approximate normality of residuals. A two-sided significance level of $\alpha = 0.05$ was used for all tests. The analyses were performed in SAS version 9.4 (SAS, Cary, NC).

3 | RESULTS

3.1 | Imaging Neurofilament Movement

A challenge to the study of neurofilament movement in axons is that these polymers measure just 10 nm in diameter and are packed close together only tens of nanometers apart, which is well below the diffraction limit of optical microscopes. To address this problem, we have taken advantage of the fact that axons in primary cultures of sympathetic or cortical neurons from neonatal rats and mice contain relatively few neurofilaments (Uchida et al., 2016). This is especially striking in cultures of neonatal cortical neurons, which extend axons that lack neurofilaments over long portions of their length (Wang and Brown, 2010). Neurofilaments that move into these gaps in the axonal neurofilament array can be observed and tracked in isolation for long distances, which is not possible in axonal regions that contain multiple overlapping neurofilaments.

For the present study, we transfected primary cultures of dissociated neonatal rat cortical neurons with GFP-tagged neurofilament protein M (GFP-NFM) and observed the cells by wide-field epifluorescence microscopy. The GFP-NFM fusion protein co-assembles freely with endogenous neurofilament proteins and incorporates along the entire length of all neurofilaments in these cells (Wang and Brown, 2010). To facilitate confirmation of axon orientation, we co-transfected the cells with EB3-mCherry, a microtubule end-binding protein that localizes to growing plus-ends. We then recorded the direction of movement of the mCherry comets in order to determine the direction of microtubule growth (Figure 1 and Movie 1 in Supporting Information Data). Because EB3 tracks the plus-ends of growing microtubules (Gouveia and Akhmanova 2010), and since axonal microtubules are organized in a predominantly plus-end distal orientation (Baas, Deitch, Black, & Banker, 1988; Heidemann, Landers, & Hamborg, 1981; Yau et al., 2016), the direction of

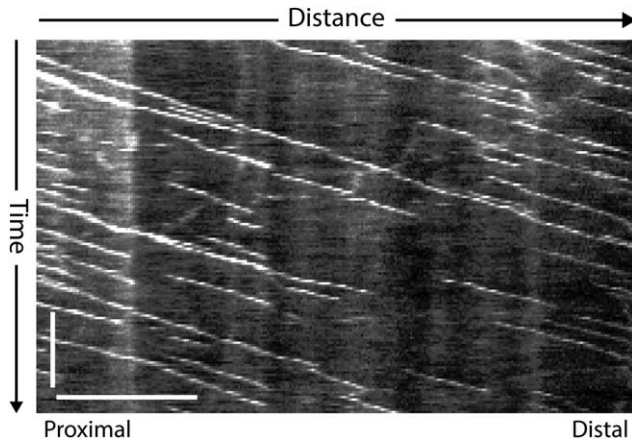


FIGURE 1 Kymograph of EB3-mCherry comets. A representative kymograph generated from the axon of a rat neonatal cortical neuron expressing microtubule end-binding protein 3 tagged with mCherry (EB3-mCherry), which tracks the plus ends of growing microtubules. The resulting microtubule “comets” reveal the direction of microtubule growth. Because nearly all axonal microtubules are organized in a plus-end-distal orientation, this also reveals the orientation of the axon. In the present study, we used this approach to establish the direction of neurofilament movements in our neurofilament kymographs (see Methods). This kymograph was generated from Movie 1 in the Supporting Information data. Horizontal scale bar, 10 μm . Vertical scale bar, 1 min

EB3-mCherry comet movement corresponded to the anterograde direction of axonal transport (Stepanova et al., 2003; Wang and Brown, 2010). Neurofilament transport data were excluded from our analysis if there was ambiguity in the axon orientation (see Methods).

To record neurofilament transport, we performed streaming acquisition at 33 frames per second with 30 ms exposures. We collected a total of 136 movies, each with a duration of either 5 or 7.5 min, corresponding to 10,000 or 15,000 frames respectively. Movie 2 (Supporting Information data) shows an example of a 7.5-min movie, down-sampled to minimize the file size and playback time, and Supporting Information Movie 3 shows an excerpt from that movie in real time with no down-sampling.

3.2 | Kymograph Analysis

Kymograph analysis (Waterman-Storer, Desai, Bulinski, & Salmon, 1998) is a sensitive method for the analysis of axonal transport in cell culture because the narrow width of the axons (close to the diffraction limit) constrains the movement of the cargo along an effectively linear path. To analyze the kinetics of neurofilament movement, we generated kymographs along all the axons that exhibited neurofilament movement in the acquired movies (Figure 2). A total of 301 kymographs were generated, from an average of 2.2 axons per movie (e.g., Movie 2 in Supporting Information data). For consistency, we always traced the paths for kymograph generation in a proximal-to-distal direction so that anterograde movements appeared left-to-right in the kymographs, and retrograde movements appeared right-to-left. The width of the kymographs was limited by the length of the axon traced

within the camera field of view, and ranged from 11 to 162 μm (67 to 1,013 pixels). The height of the kymographs was dictated by the duration of the streaming acquisition, which was either 5 or 7.5 min

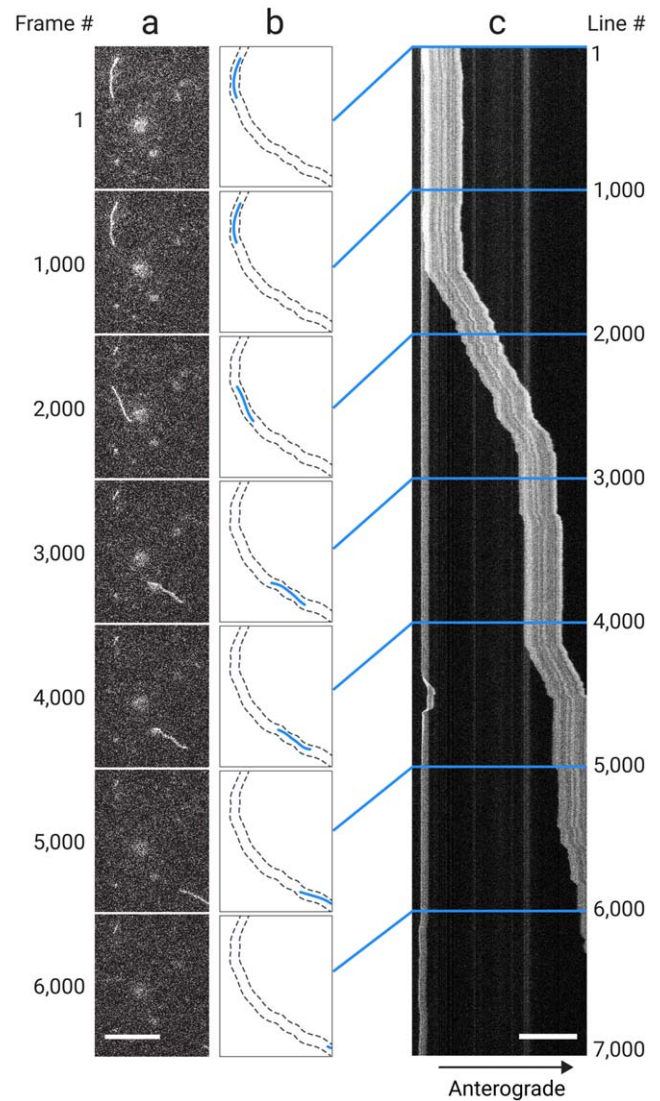


FIGURE 2 Neurofilament kymograph generation. Kymograph analysis transforms a movie into a two-dimensional image based on a line drawn along the projected path of neurofilament movement. This figure illustrates kymograph generation for a short length of axon from a 7,000-frame excerpt of one of our movies. (a) Still frames from the movie showing a neurofilament moving across the camera field of view (see Movies 2 and 3 in Supporting Information data). (b) Drawings of the neurofilament shown in (a). The dashed lines demarcate the 5 pixel-wide path that was sampled to generate the kymograph (see Methods). (c) The resulting neurofilament kymograph. The width of the kymograph, which represents distance along the axon, corresponds to the length of the axon path shown in (b). The height of the kymograph represents elapsed time, with each row of pixels coming from one frame (30.3 ms) of the movie. The decrease in the intensity of the filament over time is due to photobleaching (see text). Scale bars, 20 μm [Color figure can be viewed at wileyonlinelibrary.com]

(10,000 or 15,000 rows). By attenuating the intensity of the exciting light, we were able to reduce the amount of photobleaching, thus allowing the fluorescent filaments to remain visible for thousands of

frames (e.g., Figure 2c). To estimate the extent of photobleaching, we analyzed 8 filaments that could be tracked for a minimum of 8,000 frames within their respective kymographs (average = 13,635 frames,

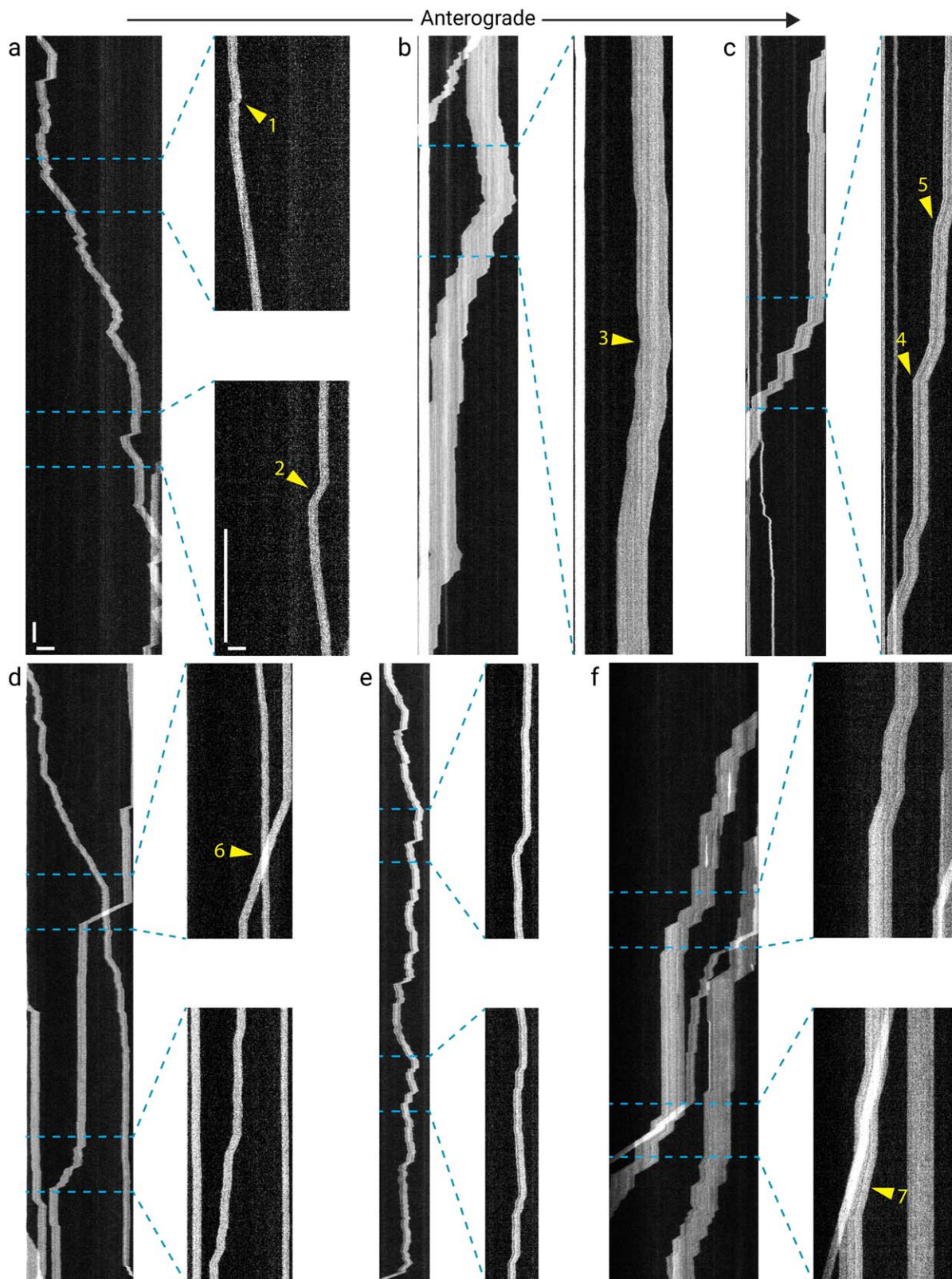


FIGURE 3.

6.9 min of continuous illumination). On average, the fluorescence intensity of these filaments decreased by 52% over 15,000 frames.

Figure 3 shows representative examples of neurofilament kymographs. Because of their length, the neurofilaments appear as ribbons or broad stripes, rather than the thin lines that are commonly encountered in kymographs of membranous vesicles. The stripes are vertical when the filaments are pausing and at an angle with respect to the vertical when they are moving, with the magnitude of the slope yielding the velocity. As reported previously, both anterograde and retrograde movements were observed (Uchida and Brown, 2004; Uchida et al., 2009; Wang and Brown, 2001, 2010; Wang et al., 2000). The filaments varied in brightness, presumably reflecting variation in the expression level of the GFP-NFM fusion protein. When filaments crossed paths, which was common, the increase in brightness was equal to the sum of the intensities of the overlapping filaments (see arrowhead in Figure 3d).

We often observed bright or dark vertical stripes superimposed on the filament trajectories in the kymographs. In some cases, it was clear that these stripes were independent of the filaments and were caused by unevenness in the background fluorescence along the axon or overlap with other fluorescent filaments because they remained fixed during filament movement (e.g., Figure 3b). However, in many cases we also observed stripes that paralleled the movement of the filaments, indicating that they represented non-uniformities in the fluorescence along the filaments themselves (e.g., Figures 2c and 3c). We refer to this phenomenon as “barcoding” because it gives the filament trajectories the appearance of a product bar code. A practical benefit of this “barcoding” appearance is that it provides fiducial marks along the filaments that can help to confirm filament orientation and to distinguish the filaments from each other when their trajectories are obscured due to filament overlap. Notably, the barcode pattern of each filament persisted during both runs and pauses (e.g., Figure 3f), indicating that it was not simply a “scrunching” of the polymer.

3.3 | Description of the Kinetic Behavior

Qualitatively, the kymographs reveal several noteworthy features of neurofilament movement. First, the filaments exhibited considerable diversity and complexity to their movement, with some moving rapidly

and intermittently in a persistent anterograde or retrograde direction (e.g., Figure 3f) and others exhibiting multiple reversals (e.g., Figure 3a), sometimes shuttling forwards and backwards with no apparent preferred direction of movement (e.g., Figure 3e). Second, the motion was intermittent and highly asynchronous, with each filament moving and pausing independently of its neighbors. Moving filaments often passed pausing filaments or moved past each other in opposite directions (e.g., Figure 3d). Third, the filaments are flexible and sometimes exhibited complex folding behaviors (not shown here), but as noted previously they almost always stretched out when they moved (Taylor, Wang, & Brown, 2012). The details of this folding behavior will be described in a future publication. Fourth, the filaments exhibited two kinds of transitions between running and pausing states. Some were abrupt, giving rise to sharp angles in the kymograph trajectories that reflect rapid acceleration or deceleration of the filament within one or two time intervals (e.g., arrowhead 4 in Figure 3c), whereas others were gradual, giving rise to curved angles reflecting a gradual acceleration or deceleration lasting a number of time frames (e.g., arrowhead 5 in Figure 3c). Fifth, a single filament could exhibit different velocities in consecutive bouts of movement (Figure 3c). Sixth, while sustained reversals were relatively rare (e.g., arrowhead 3 in Figure 3b), transient reversals were common (e.g., arrowhead 2 in Figure 3a).

3.4 | Extraction of Filament Trajectories

To detect the edges of the filaments in the kymographs, we used the Canny-Deriche edge detection algorithm (Deriche, 1987). We only included filaments that had two edges visible for at least some portion of the kymograph. Because of the low signal-to-noise ratio of our images, the algorithm identified numerous spurious edges that arose from random noise or from non-uniformities in the GFP fluorescence along the filaments. For relatively bright neurofilaments (high signal-to-noise ratio), the non-maximum suppression feature of the algorithm clearly separated the long continuous edges of the neurofilaments from these short spurious edges (Figure 4a). For fainter filaments (medium or low signal-to-noise ratio), one or both edges were less distinct and the nonmaximum suppression was weaker, sometimes

FIGURE 3 Examples of neurofilament kymographs. The kymograph excerpts shown here were selected to show the diversity of the neurofilament motile behavior. The kymographs in (a, b, c, d, e, and f) are each 5,000 rows in height (2.5 min in time). The kymographs in b and c are each accompanied by one magnified region (denoted by dashed blue lines) that is 900 rows in height (27 s in time). The kymographs in (a, d, e, and f) are each accompanied by two magnified regions (denoted by dashed blue lines) that are 400 rows in height (12 s in time). The yellow arrowheads mark features of interest, which are described here and in the text. (a) A filament (length $\approx 5.3 \mu\text{m}$) that moved in a net anterograde direction but exhibited numerous short reversals (arrowheads 1 and 2 in a). (b) A filament (length $\approx 17.6 \mu\text{m}$) that moved in a net anterograde direction and then reversed (arrowhead 3 in b) and moved in a net retrograde direction. Note that the subtle barcoded appearance of this filament (see text) is obscured by more prominent vertical stripes, which clearly represent non-uniformities in the background fluorescence along the axon because they remained fixed relative to the moving filament. (c) A filament (length $\approx 8.8 \mu\text{m}$) that moved in a net retrograde direction, alternating between runs of varying velocity and duration and pauses of varying duration. Note that the transitions between the runs and pauses could be abrupt and angular (e.g., arrowhead 4 in c) or gradual and rounded (e.g., arrowhead 5 in c). Also note the barcoded appearance of the filament in (c). (d) A filament (length $\approx 4.2 \mu\text{m}$) moving in a net anterograde direction crossed paths with a filament (length $\approx 4.8 \mu\text{m}$) moving in a net retrograde direction. The region of overlap is evident from the increase in brightness (arrowhead 6 in d). (e) A filament (length $\approx 4.3 \mu\text{m}$) that exhibited numerous repeated reversals with no clear directional preference. (f) Three filaments (lengths $\approx 13.3, 5.3,$ and $15.4 \mu\text{m}$) that all moved in a net retrograde direction, overlapping occasionally. Note that the overlapping short and long filaments marked by arrowhead 7 in (f) moved at the same run velocity. Also note the barcoded appearance of the filament in (f). Horizontal scale bars, $10 \mu\text{m}$. Vertical scale bars, 5 s [Color figure can be viewed at wileyonlinelibrary.com]

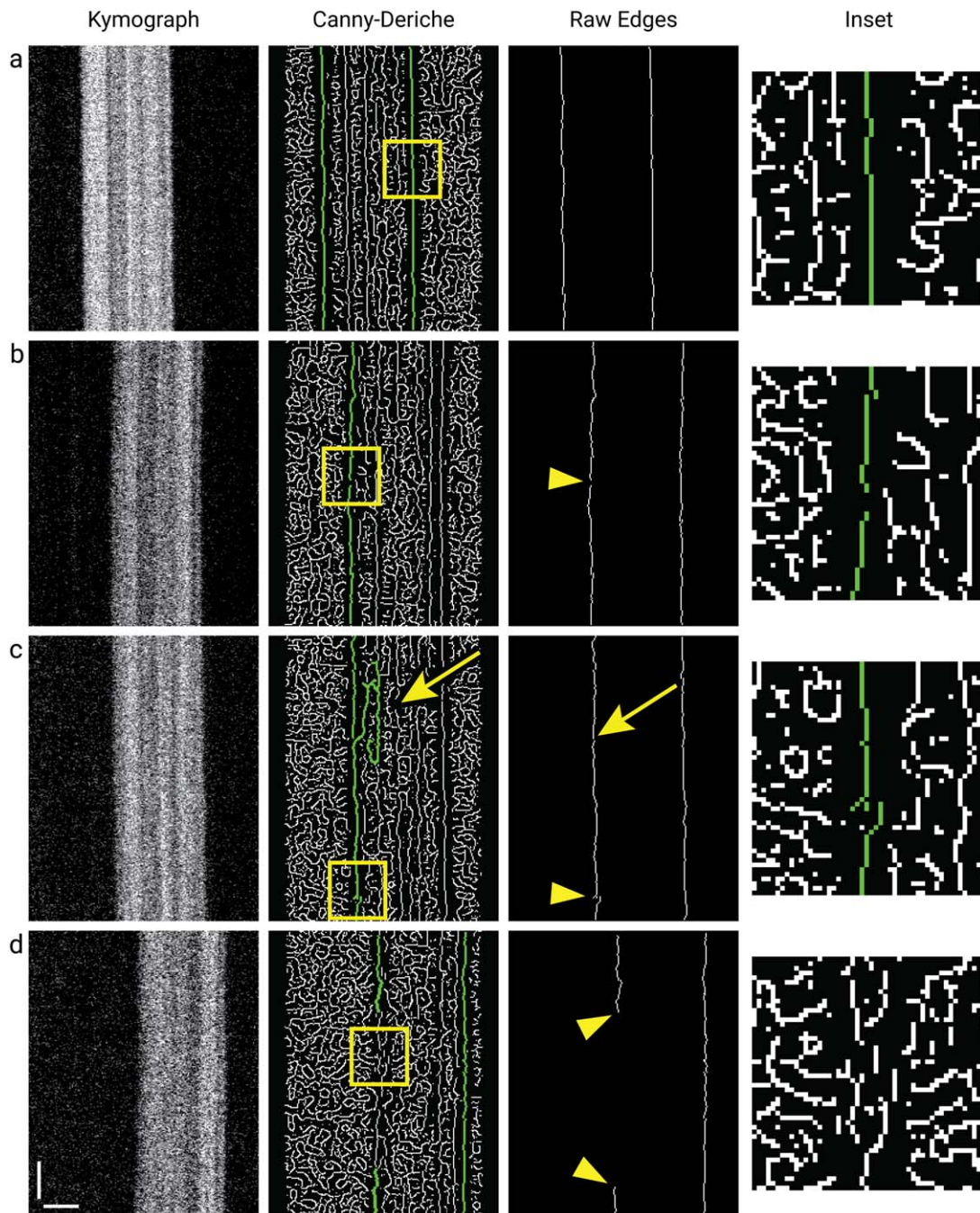


FIGURE 4 Edge detection using the Canny-Derliche algorithm. (a) Example of continuous neurofilament edges (highlighted in green) flanked by strong edge suppression channels in an image with a relatively high signal-to-noise ratio. (b) Example of a short gap (arrowhead and inset) in the proximal edge of a neurofilament with a lower signal-to-noise ratio. The frequency of such gaps increased with decreasing signal-to-noise ratio. (c) Examples of branching in the proximal edge of neurofilament, arising due to failure of non-maximum edge-suppression. Small branches (arrowhead and inset) were not edited and were averaged later in the processing. Longer branches (arrow) were rare and were the only edited feature in our final Raw Edges (see Methods). (d) In areas of relatively low signal-to-noise ratio, or in areas where two filaments overlapped, edge detection sometimes failed completely leaving very long gaps in the neurofilament edges (arrowheads). The yellow boxes mark the areas shown at higher magnification in the insets. The pixelation of the images is evident at this higher magnification. Horizontal scale bar, 5 μm . Vertical scale bar, 1 s [Color figure can be viewed at wileyonlinelibrary.com]

resulting in gaps in the neurofilament edges (Figure 4b,d). Gaps could also arise due to overlap with other filaments in the axon. We considered the possibility of filling in such gaps by interpolation, but chose not to do so in order to avoid bias and to minimize manipulation of the

raw data. Occasionally the Canny-Derliche algorithm generated multiple or branched edges for a single filament end due to fusion of the neurofilament edges with surrounding spurious edges (e.g., Figure 4c). These features were either edited manually according to strict criteria or they

were eliminated automatically during the subsequent processing by averaging their position to create a single edge (see Methods).

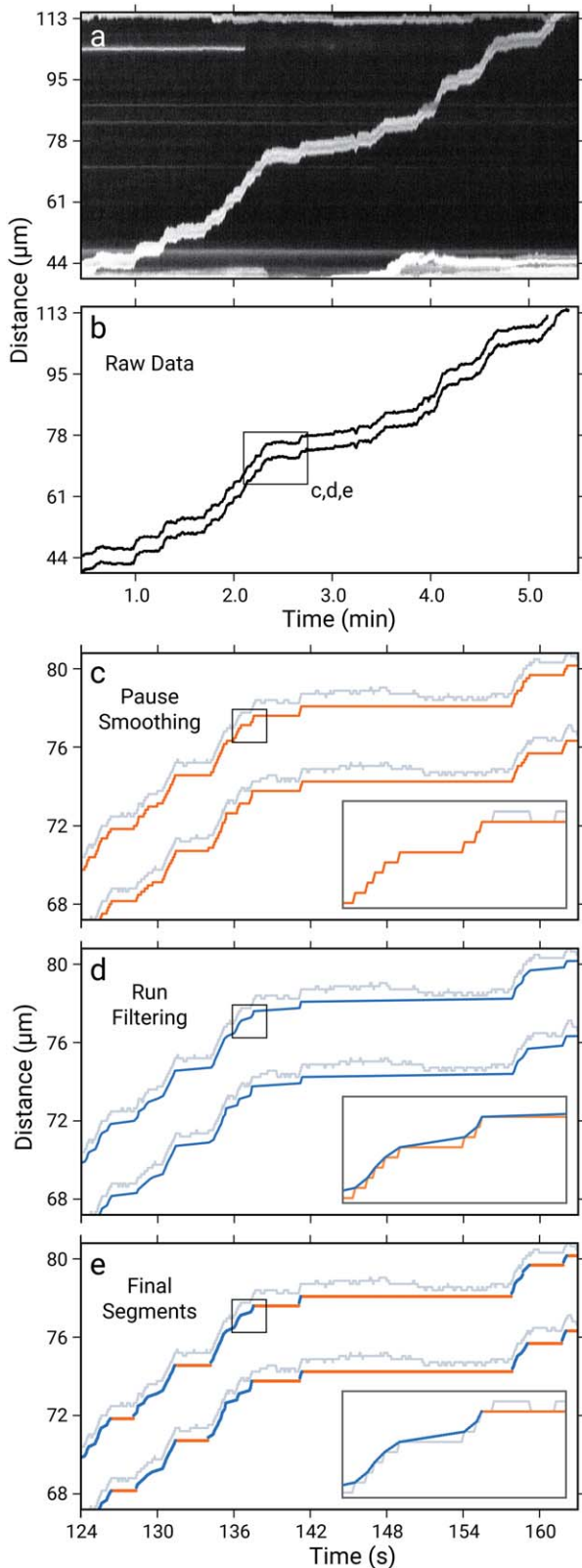


FIGURE 5.

Because the Canny–Deriche algorithm operates independently on each filament end, and since the two ends of a filament can differ in their brightness, it was not unusual to encounter gaps in the detected edge at one end of a filament but not the other (e.g., Figure 4d). Further, given the flexibility of these polymers, the motion of the two ends of each filament was not always correlated precisely. Thus, we treated the trajectories of the two ends of each filament as independent events in the subsequent analysis.

3.5 | Identification of Runs and Pauses

The spatial resolution of our movies was limited by the pixel dimensions (160 nm) of our camera and the speed of image acquisition (33 frames per second). Thus, each bout of movement appeared in the kymographs as a series of pixel stair steps, with each step a minimum of 160 nm in the horizontal (spatial) dimension and 30.3 ms in the vertical (temporal) dimension. In addition, due to the nature of low-light imaging, the trajectories of the filament edges were inherently noisy. This pixelated and noisy data presented a challenge for defining runs and pauses in the extracted traces. To address this objectively, we developed an automated pause-smoothing/run-filtering computational algorithm (Figure 5; see Methods).

In the first “pause-smoothing” step of this algorithm, we sampled each trace thousands of times to find all segments of the traces that might qualify as pauses, defined as intervals during which the filament end started and ended in the same location and deviated by less than ± 2 pixels in between. The algorithm then smoothed out these potential pauses by resetting all the points within each qualifying interval to the average for that interval, rounded to the nearest integer value. The

FIGURE 5 Extraction of runs and pauses. This figure illustrates the major steps in the pause-smoothing/run-filtering computational algorithm that was used to identify moving and pausing segments in our neurofilament trajectories (see Methods). (a) A raw kymograph, rotated so that the x axis is time and the y axis is distance. (b) The raw trajectories of the two filament ends, obtained using the Canny–Deriche edge detection algorithm. The region inside the box is shown in more detail in (c, d, and e). (c) The result of the “pause-smoothing” step overlaid on the raw data, which is offset to facilitate visual comparison. This step is an iterative process that identifies and “smooths out” potential pauses based on a noise threshold. The inset in (c) shows a portion of the pause-smoothed trace overlaid on the raw data trace with no offset. (d) The result of the first part of the “run-filtering” step overlaid on the raw data, which is offset to facilitate visual comparison. In this step, the corners of each pause segment in (c) are connected linearly “corner-to-corner,” turning the entire trace into a series of contiguous runs. The inset in (d) shows a portion of this contiguous-run trace overlaid on the pause-smoothed trace with no offset in order to show the connected corners. (e) The final result of the run-filtering step overlaid on the raw data, which is offset to facilitate visual comparison. This shows the pause and run segments identified by applying the velocity cut-off filter to the traces in (d). The inset in (e) shows a portion of this final trace overlaid on the raw data trace with no offset. The run and pause segments and raw data are depicted in blue, orange and grey, respectively, throughout. [Color figure can be viewed at wileyonlinelibrary.com]

result was a series of traces consisting of alternating flat intervals and runs (Figure 5c). We refer to these smoothed intervals as “potential” pauses because the actual final segmentation of the traces into pauses and runs happened later in the process. In the second “run-filtering” step of the algorithm, we temporarily connected the corners of each “step” in the “pause-smoothed” traces, effectively transforming every segment of each trace into a potential run segment with a nonzero run velocity, and correspondingly, a nonzero slope. Each trace now resembled a series of connected run segments made up of varying slopes with all pausing segments abolished (Figure 5d).

Finally, to categorize a segment as a run or a pause, we applied a pause cut-off filter. To determine the cut-off, we created logarithmically binned bout-weighted and time-weighted frequency distributions of the speeds for all the slopes (ignoring the direction of movement). The resulting distributions both had a bimodal shape with an inflection point/minimum at $\sim 0.1 \mu\text{m s}^{-1}$ (Figure 6). This shape implied the existence of two distinct velocity states for the neurofilaments. The position of the inflection point was also similar to the 1 pixel s^{-1} ($0.0685 \mu\text{m s}^{-1}$) pause cut-off that we defined empirically in our prior studies using time-lapse imaging (Uchida et al., 2009; Wang and Brown, 2001, 2010; Wang et al., 2000). Therefore, we selected $0.1 \mu\text{m s}^{-1}$ as our pause cut-off for the present analysis and interpreted smaller speeds to be the result of noise. Accordingly, all potential runs with speeds below this threshold were reverted to pauses, and all segments with speeds above or equal to this threshold were left unchanged (see Figure 5e). Any segment with a speed of $0.1 \mu\text{m s}^{-1}$ or above was now classified as a run with an associated run time, run length and run velocity for that bout. Any segment with a speed lower than $0.1 \mu\text{m s}^{-1}$ became a pause with an associated pause time for that bout.

Examples of filament trajectories showing the assigned runs and pauses are shown in Figure 7. Note that the movement of each filament was highly intermittent, even on these very short time scales. What would have been identified as a single processive run in previous studies using time-lapse imaging with 4 or 5 s time intervals (Uchida and Brown, 2004; Wang and Brown, 2001) is now seen to actually be comprised of multiple shorter runs interrupted by short pauses (Figure 8). Comparison of the traces reveals that the filaments differed in their directionality and reversal behavior. Some filaments moved in a persistently anterograde direction with few reversals (e.g., Figure 7a,d), some moved in a persistently retrograde direction with few reversals (e.g., Figure 7c), and some reversed direction repeatedly with no apparent preferred direction of movement (e.g., Figure 7g). These observations suggest that the filaments are not all kinetically identical and that these differences can persist, at least on a time scale of several minutes.

3.6 | Algorithm Accuracy

To assess the accuracy of our computational algorithm, we quantified the discrepancy between the finalized traces and the original raw data for each time interval in the entire data set (data not shown). For

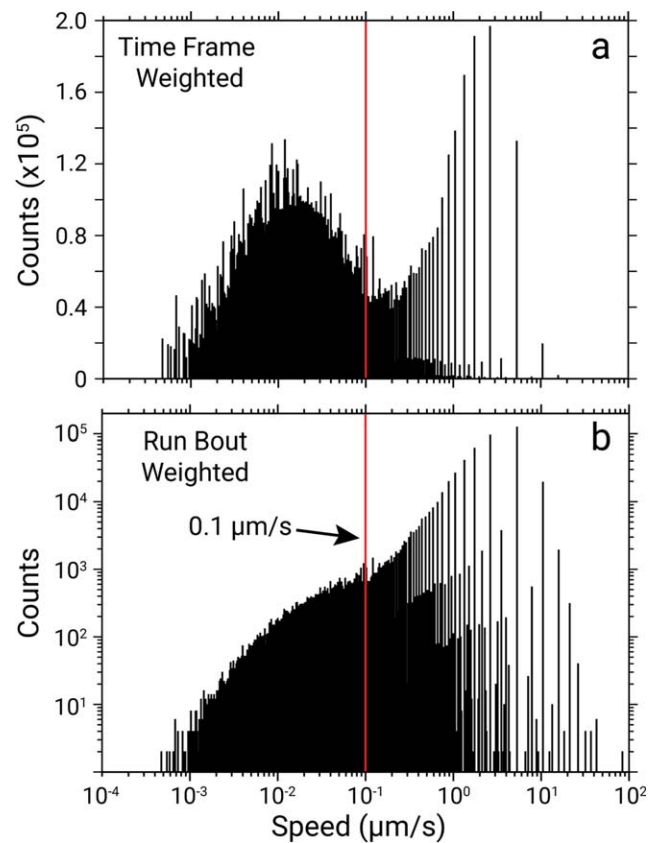


FIGURE 6 Estimation of the pause cut-off. (a) Time-weighted frequency distribution of the run speeds (weighted by run duration) generated in the run-filtering step of the algorithm (see Figure 5d), and plotted using a log-binning scheme with a linearly scaled y axis. (b) The same data recalculated as a number-weighted distribution (runs weighted equally regardless of their duration), and plotted using a log-binning scheme with a logarithmically scaled y axis. Note the bimodal distribution in both cases, with an inflection at $\sim 0.1 \mu\text{m s}^{-1}$, which we took to be our pause cut-off (see text). Runs above this threshold speed were retained as runs, while runs below this threshold were designated as pauses [Color figure can be viewed at wileyonlinelibrary.com]

moving states, the average discrepancy was 0.7 pixels, with 95.2% of all data points deviating from the raw data by ≤ 1 pixel, and a maximum deviation of 6.4 pixels. For pausing states, the average discrepancy was 0.6 pixels, with 93.2% of all data points deviating from the raw data by ≤ 1 pixel, and a maximum deviation of 4 pixels. We also tested the algorithm by generating *in silico* kymographs using a stochastic two-state model in which a filament exhibits bouts of runs and pauses with predictable average run times and pause times (data not shown). Each kymograph was based on the same model parameters, but the random number generator was re-seeded to generate multiple different, but statistically equivalent stochastic trajectories. We then coarse-grained these trajectories to the pixel size and time intervals of our experiments and analyzed them with our algorithm. The estimated average run-times, run lengths, run velocities and pause-times were within $\pm 10\%$ of the actual values.

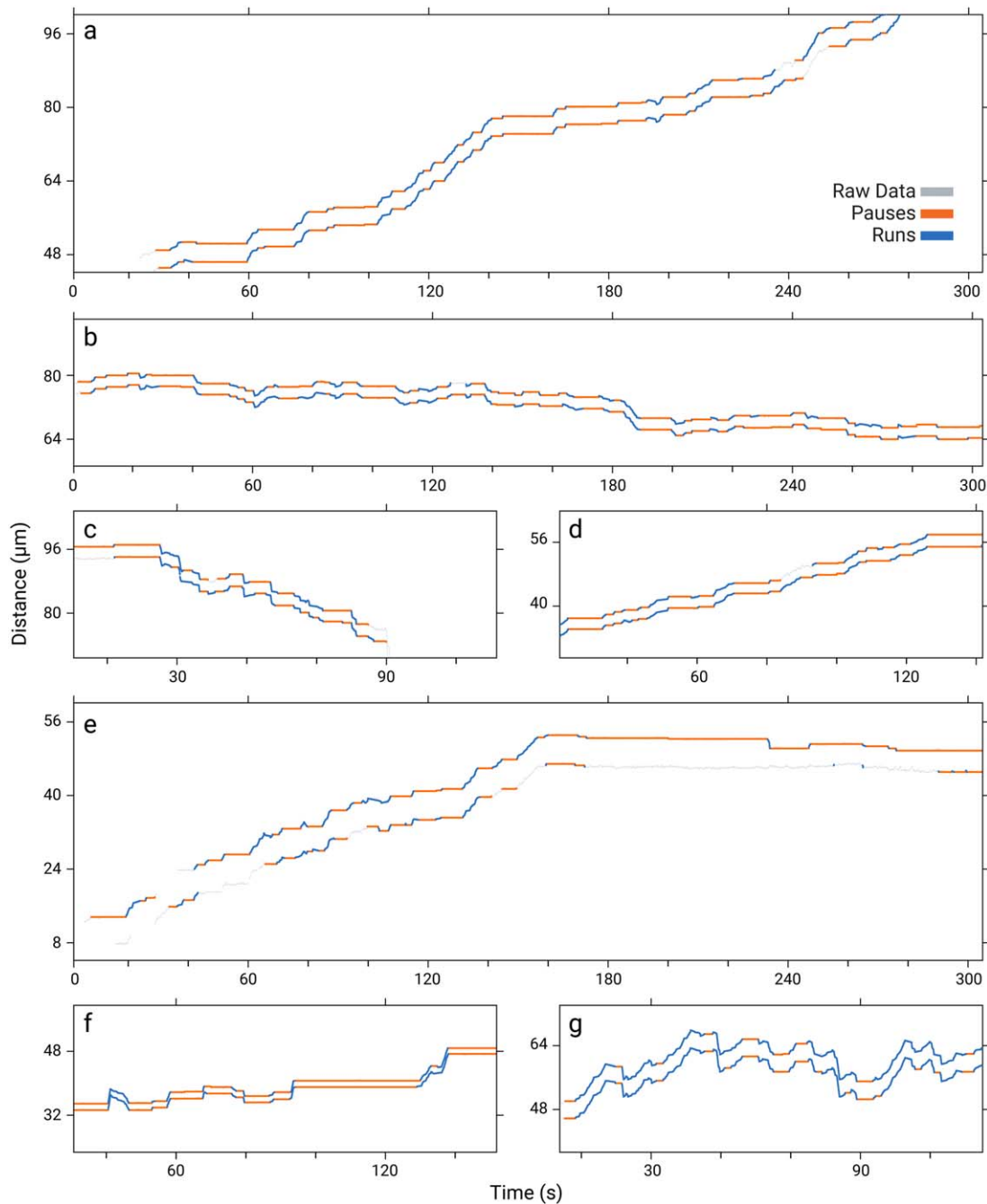


FIGURE 7 Examples of final processed filament trajectories. The computed traces are divided up into consecutive runs segments (blue) and pause segments (orange) and superimposed on the raw traces (grey). Note that the portions of the computed traces where no run or pause is assigned (grey) arise due to failure of the Canny-Derich algorithm to detect a continuous edge or, more commonly, because runs or pauses that were truncated by gaps or by the beginning or ending of the traces were rejected in order to avoid underestimating the run lengths, run times and pause times in our analysis (see Methods). (a) A filament (length $\approx 4.1 \mu\text{m}$) that moved in a predominantly anterograde direction with relatively few reversals. Note that this filament exhibited a period of alternating runs and short pauses, flanked by periods of alternating runs and longer pauses. (b,c) Two filaments (lengths ≈ 3.6 and $3.2 \mu\text{m}$, respectively) that moved in a predominantly retrograde direction but also exhibited occasional reversals resulting in short anterograde excursions. (d,e) Two filaments (lengths ≈ 2.8 and $6.2 \mu\text{m}$, respectively) that moved in a predominantly anterograde direction. The proximal (lower) end of the filament in (e) was picked up poorly by the Canny-Derich algorithm, leading to long stretches of the final trace that were not assigned as runs or pauses. (f) A filament (length $\approx 1.7 \mu\text{m}$) that moved in a net anterograde direction with relatively long intervening pauses. (g) A filament (length $\approx 4.3 \mu\text{m}$) that exhibited numerous reversals with alternating anterograde and retrograde runs and no preferred direction of movement. All plots are scaled equally in both time (x axis) and distance (y axis) [Color figure can be viewed at wileyonlinelibrary.com]

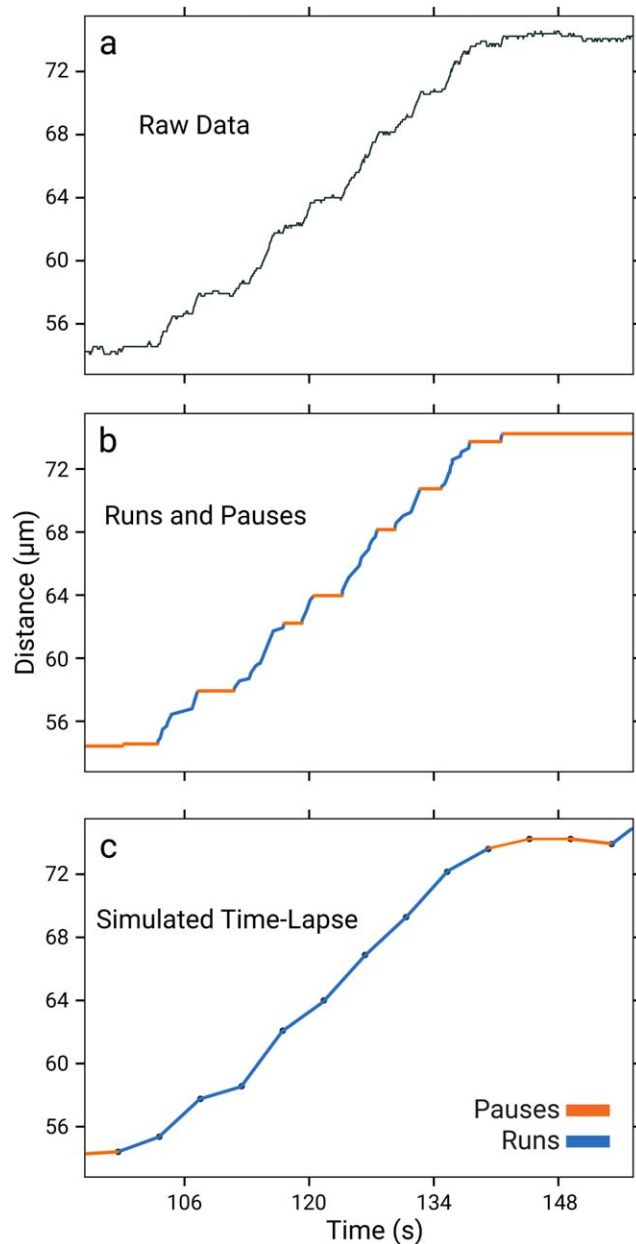


FIGURE 8 Time-lapse imaging fails to detect the short runs and pauses. (a) The raw trace obtained for a single neurofilament end in the current study using streaming acquisition with 30.3 ms temporal resolution. (b) The assigned runs (blue) and pauses (orange), obtained using our pause-smoothing/run-filtering computational algorithm. (c) A simulation of how the filament trajectory would appear if tracked using time-lapse imaging. The data points in A were averaged over a 1 second interval every 5 s to simulate 1-s exposures with 5-s time intervals, similar to the imaging conditions that we have used in our previous time-lapse imaging studies (Uchida and Brown, 2004; Wang and Brown, 2001; Wang et al., 2000). To be consistent with those prior studies, runs and pauses in this simulated time-lapse trace were assigned using a pause cut-off of $0.16 \mu\text{m s}^{-1}$ (1 pixel s^{-1}). Using time-lapse imaging, this filament would have appeared to exhibit a single $\sim 17 \mu\text{m}$ run instead of numerous short alternating runs and pauses [Color figure can be viewed at wileyonlinelibrary.com]

3.7 | Movement Kinetics

In total, we applied the above computational algorithm to the trajectories of the proximal and distal edges of 726 filaments (1,452 edges in total). We then pooled these data to obtain a population-wide analysis of the filament kinetics. To match the minimum pause duration of three time intervals that was imposed by the pause-smoothing algorithm (see Methods), we excluded any runs that were less than three time intervals in duration, reducing the number of runs by 7.2%. This also minimized the vulnerability of our analysis to image and edge detection noise. The end result was a data set consisting of 11,605 anterograde runs, 10,209 retrograde runs and 15,410 pauses (Table 1). On average, the filaments spent 82.6% of their time pausing and 17.4% moving. Note, however, that this underestimates the overall pausing behavior of the axonal neurofilament population because tracking neurofilaments in gaps is biased towards the detection of moving filaments (Wang et al., 2000). In addition, the time frame of our movies is much shorter than the duration of the longest pauses, which may be 1 h or more in length (Jung and Brown, 2009; Li, Brown, & Jung, 2014; Li et al., 2012; Trivedi, Jung, & Brown, 2007). Consistent with previous reports of an anterograde bias to neurofilament transport (Wang and Brown, 2001; Wang et al., 2000), the moving filaments spent an average of 55.9% of their time moving anterogradely.

To further characterize the motile behavior, we plotted frequency distributions of the pause times, run lengths, run times and run velocities (Figure 9). The average values are shown in Table 2. The average pause time was 9.3 s and the longest pause recorded was 381 s. Run lengths and run times ranged from 0.08 to 29.0 μm (with an average of $\bar{x} = 0.94 \mu\text{m}$) and 0.03 to 25.5 s (with an average of $\bar{t} = 1.46 \text{ s}$), respectively, for anterograde bouts of movement, and from 0.08 to 30.8 μm

TABLE 1 Summary of the dataset collected in this study

Data type	Sample size
Movies	136
Kymographs	301
Filaments analyzed	726
Proximal edge traces	16,341
Distal edge traces	17,489
Total raw data points collected	8,639,333
Total raw time collected	72.7 hours
Total filtered data points analyzed	5,572,121
Total filtered time analyzed	46.9 hours
Pausing segments	15,410
Anterograde segments	11,605
Retrograde segments	10,209

The proximal and distal edge traces represent the traces extracted from the raw data generated by the Canny-Deriché edge detection algorithm. Pausing segments and anterograde or retrograde segments are the single kinetic bouts (pauses and runs) computed by the pause-smoothing/run-filtering algorithm.

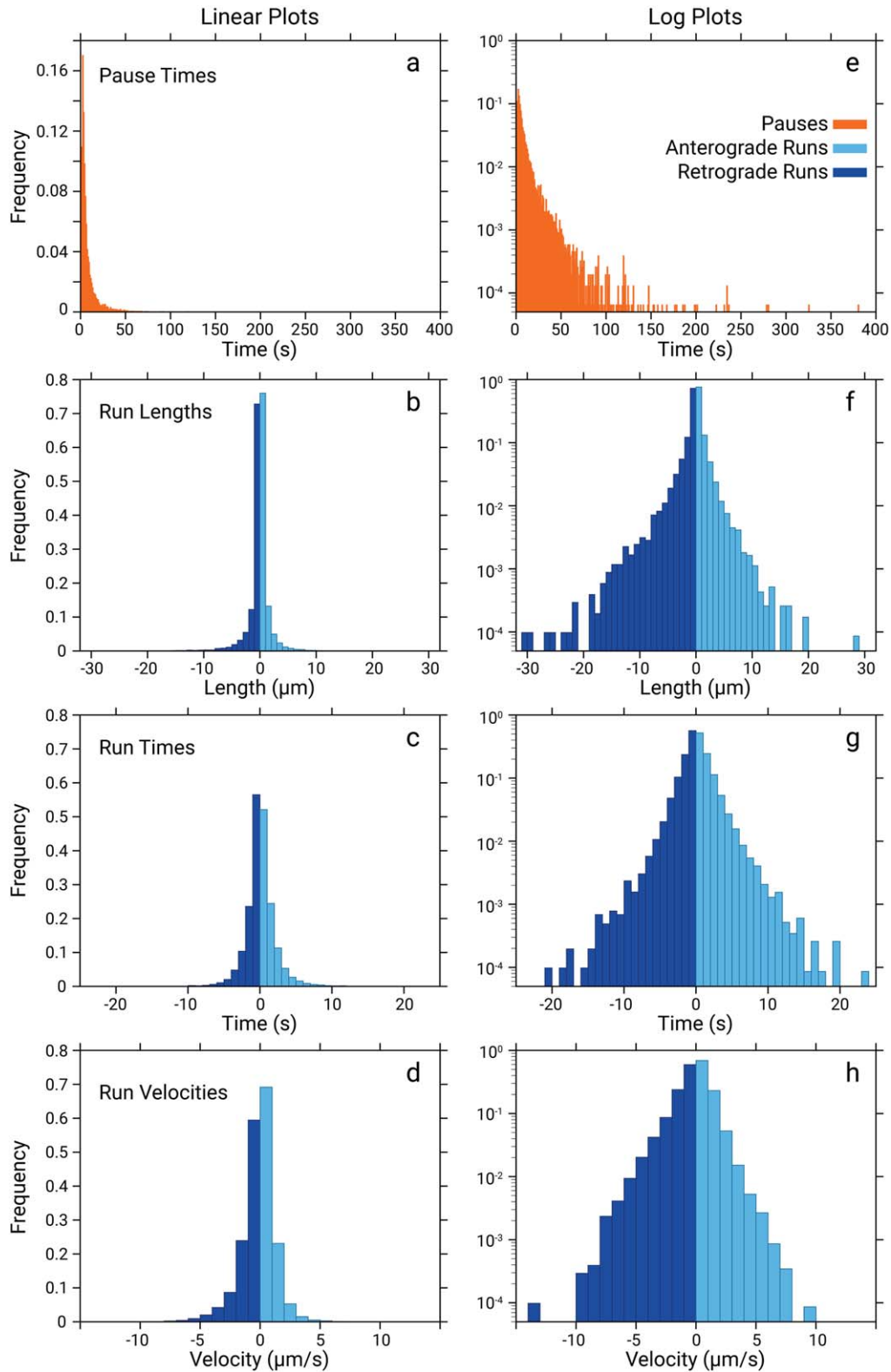


FIGURE 9 Frequency distributions of the kinetic parameters. (a–d) Linear plots. (e–h) Logarithmic plots. The frequency on the y-axis represents the fraction of the total pause or run segments. (a,e) Pause times. The vast majority of the pause times were <50 s with an average pause time of 9.3 s. (b,f) Run Lengths. Average retrograde and anterograde run lengths were 1.19 and 0.94 μm , respectively. (c,g) Run Times. Average retrograde and anterograde run times were 1.31 s and 1.46 s respectively. (d, h) Run Velocities. Average retrograde and anterograde velocities were 1.18 and 0.89 $\mu\text{m s}^{-1}$, respectively. The difference in the average run length, run time and run velocity for anterograde and retrograde movements is consistent with reports that different directions of neurofilament movement are powered by distinct molecular motors (Uchida et al., 2009) [Color figure can be viewed at wileyonlinelibrary.com]

TABLE 2 Summary of the kinetic analysis

	Avg	Min	Max
Anterograde kinetics			
Run length (μm)	0.94	0.08	28.96
Run time (s)	1.46	0.03	25.54
Velocity ($\mu\text{m s}^{-1}$)	0.89	0.1	6.6
Retrograde kinetics			
Run length (μm)	1.19	0.08	30.84
Run time (s)	1.31	0.03	20.63
Velocity ($\mu\text{m/s}$)	1.18	0.1	7.8
Pausing kinetics			
Pause time (s)	9.32	1.6	381
Length information			
Filament Length (μm)	5.5	0.6	42.1
Motile state			
Time pausing	82.6%		
Time moving	17.4%		
Anterograde	55.9%		
Retrograde	44.1%		

Note that the minimum velocities, run lengths, run times and pause times are defined by our chosen cut-offs ($0.1 \mu\text{m s}^{-1}$ and 1.6 s) and frame rate (30.3 ms). The maximum velocities reported are for bouts that were sustained for greater than 10 time frames (330 ms).

(with an average of $\bar{x} = 1.19 \mu\text{m}$) and 0.03 to 20.6 s (with an average of $\bar{x} = 1.31 \text{ s}$), respectively, for retrograde bouts of movement. Run velocities averaged $0.89 \mu\text{m s}^{-1}$ for anterograde movements and $1.18 \mu\text{m s}^{-1}$ for retrograde movements. Maximum run velocities were $9.2 \mu\text{m s}^{-1}$ anterograde and $13.2 \mu\text{m s}^{-1}$ retrograde, but these high velocities corresponded to single bouts of movement (out of a total of $>20,000$ runs) that were each sustained for just four-time intervals (121 ms). In total, we found 46 anterograde and 170 retrograde bouts that were in excess of $5 \mu\text{m s}^{-1}$ (with average durations of 5.4 and 14.6 time frames, respectively). For runs that were sustained for at least 10 time intervals (303 ms), the maximum run velocities were $6.6 \mu\text{m s}^{-1}$ anterograde and $7.8 \mu\text{m s}^{-1}$ retrograde (Figure 10).

3.8 | Dependence of the Transport Kinetics on Filament Length

We have reported previously that moving neurofilaments in cultured neurons range widely in length (Uchida and Brown, 2004; Uchida et al., 2009; Wang and Brown, 2001, 2010; Wang et al., 2000). Because it is possible that longer filaments experience more drag, we investigated whether there was any length-dependence to the transport kinetics described above. To measure neurofilament length during each kinetic bout, we created a subset of the data obtained from our pause-smoothing/run-filtering algorithm that included only time points for

which there was positional information available simultaneously for both filament ends. Because of the flexibility of the polymers it is possible for their two ends to be in different kinetic states at the same time for a limited number of time frames. For example, this can arise if a filament is not fully outstretched at the start of a run or if a filament folds back on itself during a run. To address this, we further narrowed the data set to include only portions of the traces where data was available for both ends of the filament and where those two ends were in the same kinetic state (moving or pausing). This resulted in a dataset of “common runs” and “common pauses” that was then analyzed using the same algorithm techniques described above, except now each kinetic bout had an associated filament length. These additional selection criteria reduced the size of the overall data set by 28%, from 5.57×10^6 data points to 4.0×10^6 , representing 709 different filaments. Finally, we averaged the run velocities, run lengths, run times and pause times of the two ends of each filament for each kinetic bout in order to simplify the statistical analysis.

To obtain the filament lengths, we calculated the average distance between the two filament ends during each kinetic bout (run or pause). The resulting lengths ranged from 0.6 to $42.1 \mu\text{m}$, with an average length of $5.5 \mu\text{m}$ (Figure 11). Figure 12 shows the kinetic parameters (pause time, run length, run time and run velocity) plotted in three ways: (1) a histogram of the average parameter values versus filament length using $2 \mu\text{m}$ bins, (2) a scatter plot of the data points versus filament length, and (3) a scatter plot of the natural logarithm of the data points versus filament length. The scatter plots show a wide range of values for each kinetic parameter at any given filament length. Predictably, the range was larger at short lengths because short filaments were more numerous in our data set and thus we have more runs and pauses for short filaments (refer to the overall filament length distribution in Figure 11). Visual inspection of the histograms reveals some noise in the data, but no obvious decrease in the kinetic parameters with increasing length for pauses or for anterograde or retrograde runs. To test this statistically, we used mixed effects modeling with a natural log transformation of the run velocities, run lengths, run times and pause times to better approximate normality of the residuals (see Methods). We found an effect of filament length on run velocity and run length that was different between anterograde and retrograde runs ($p = 0.0002$ and $p = 0.001$ for run velocity and run length, respectively). Greater filament length was associated with increased run velocity ($p < .0001$) and increased run length ($p < .0001$) for retrograde runs, but not for anterograde runs ($p = 0.98$ and $p = 0.21$ for run velocity and run length, respectively). Greater filament length was also associated with increased run time ($p = 0.045$). While this effect was not different between anterograde and retrograde runs ($p = 0.27$), inspection of the slopes of the regression lines generated by the statistical analysis and superimposed on the natural-log transformed scatter plots in panels l and o of Figure 12 suggest that the retrograde filaments contributed most to this dependence. There was no association between filament length and pause time ($p = 0.59$).

This analysis indicates that there was no decrease in run velocity, run length or run time with increasing filament length, and surprisingly, that there was an increase in these parameters with respect to filament length for retrograde filaments. The magnitude of this increase can be

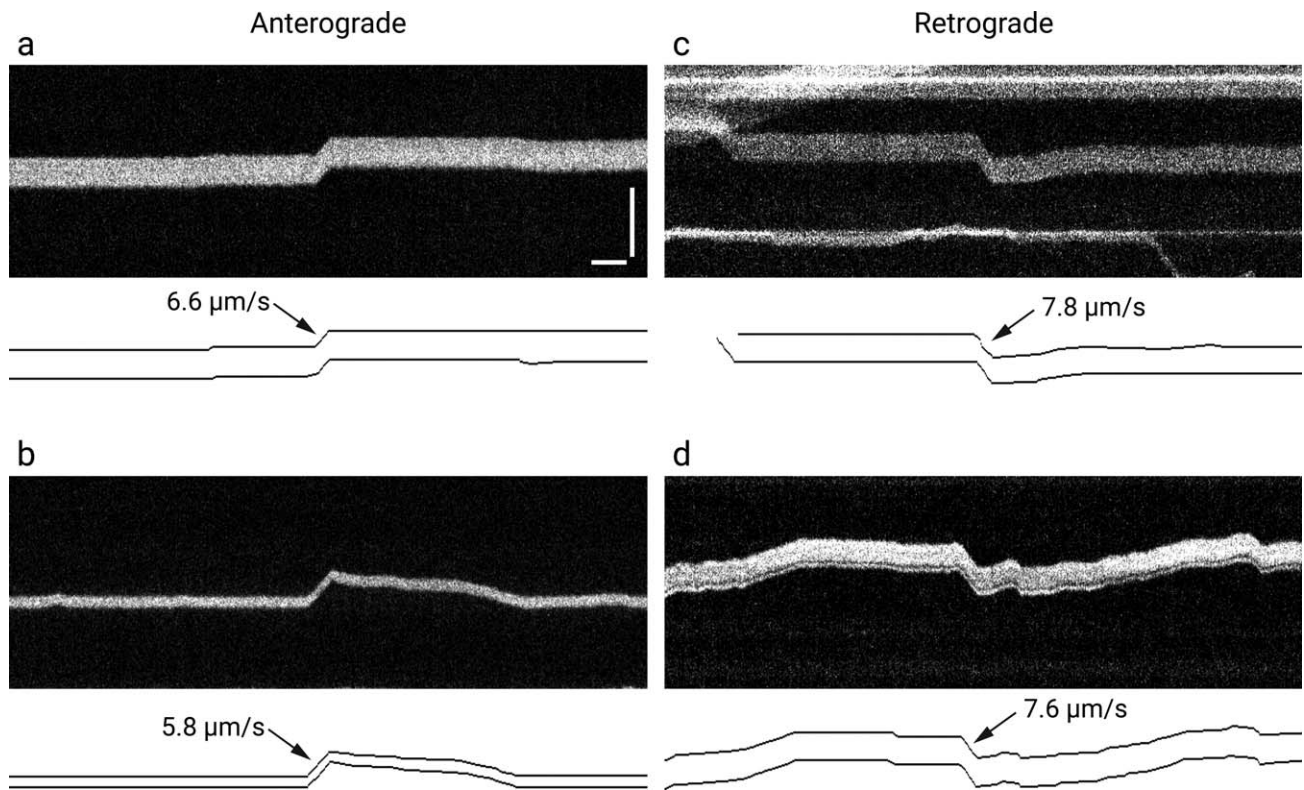


FIGURE 10 The fastest neurofilament movements. (a,b) The two fastest anterograde movements that were sustained for at least 330 ms (10 time frames). The filament lengths were ~ 4.5 and $1.8 \mu\text{m}$, respectively. The run times of the bouts (arrows) were 455 and 636 ms (15 and 21 time frames) respectively. (c,d) The two fastest retrograde movements that were sustained for at least 330 ms (10 time frames). The filament lengths were ~ 4.2 and $4.3 \mu\text{m}$, respectively. The run-times of the bouts (arrows) were 424 and 576 ms (14 and 19 time frames) respectively. The kymographs are rotated so that distance is in the vertical dimension and time is in the horizontal dimension. The traces beneath each kymograph represent the trajectories of the two ends of the filament of interest. Horizontal scale bar, 1 s. Vertical scale bar, $10 \mu\text{m}$

seen in the positive slope of the regression lines generated by the statistical analysis and superimposed on the natural-log transformed scatter plots in panels f, l, and r in Figure 12. For example, the analysis shows that $25\text{-}\mu\text{m}$ -long retrogradely moving filaments moved $\sim 50\%$ faster (average = $1.53 \mu\text{m s}^{-1}$) than $5\text{-}\mu\text{m}$ -long retrogradely moving filaments (average = $1.03 \mu\text{m s}^{-1}$; Figure 12r), whereas for anterogradely moving filaments there was no length-dependence (Figure 12u).

4 | DISCUSSION

Neurofilaments are unique among the known cargoes of axonal transport in that they are protein polymers just 10 nm in diameter but many micrometers in length. In the present study, we have imaged these cargoes by streaming acquisition at low light levels using 30 ms exposures for $5\text{--}7.5 \text{ min}$ ($10\text{--}15,000$ frames) without excessive photobleaching. This has enabled us to perform the first kymograph analysis of neurofilament transport with >100 fold better temporal resolution than in our previous time-lapse imaging studies. To locate the filament ends, we used an edge detection image processing algorithm. To identify bouts of movement and pausing in the resulting pixelated traces, we developed a novel automated pause-smoothing/run-filtering computational algorithm. By automating this process, we were able to analyze the

trajectories of 726 filaments, representing a total of 37,224 distinct moving and pausing events, which is far more than would be practical using manual methods. We then pooled these data to analyze the distributions of the run velocities, run times, run lengths and pause times for the filament population. Several other laboratories have described automated computational algorithms for tracking moving objects in kymographs, including edge detection methods (Chaphalkar, Jain, Gangan, & Athale, 2016; Zhang, Osakada, Xie, & Cui, 2011), but our procedure differs in that it is a data-driven solution to the specific problem of identifying runs and pauses in pixelated and noisy traces. Our analysis of this new data set revealed new features and complexity to the transport kinetics which are discussed below.

4.1 | The Maximum Velocity of Neurofilament Transport

Inspection of the filament trajectories revealed that neurofilament movement is more intermittent than was previously apparent. Specifically, the bouts of movement that appeared to be continuous for periods of tens of seconds or minutes in our previous time-lapse imaging studies actually consist of multiple alternating short runs and pauses, with run velocities appreciably faster than previously measured and run lengths appreciably shorter. For example, our analyses of neurofilament

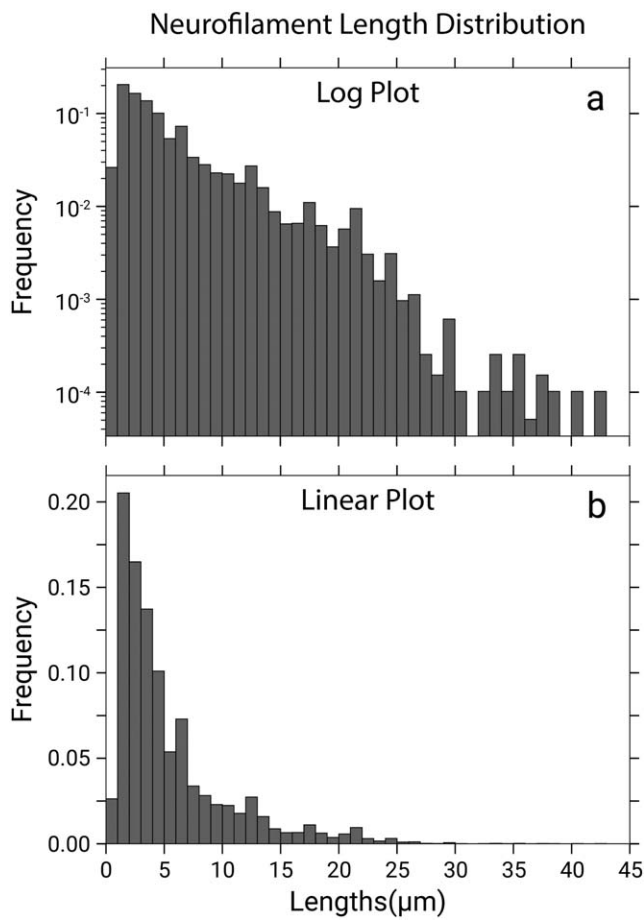


FIGURE 11 Filament length distribution. (a) Bout-weighted frequency distribution of filament lengths for all runs and pauses for which data was available for both ends of the filament and for which both ends were in the same kinetic state (total = 13,492 segments), semi-log plot. (b) The same data on a linear plot. The filament lengths ranged from 0.6 to 42.1 μm with an average length of 5.5 μm . Interestingly, mixed effects modeling of the lengths separated out into runs and pauses (data not shown) revealed that filaments were longer during runs than during pauses ($p < 0.0001$), but the magnitude of the difference in the estimated mean lengths was only 2.1% for anterograde runs and 1.3% for retrograde runs. While these differences are small, they could reflect a slight “straightening out” of the filaments when they were acted on by molecular motors

transport in cultured neurons using time-lapse imaging with 4 or 5 s time intervals yielded average run velocities of $\sim 0.4 \mu\text{m s}^{-1}$ anterograde (range = $0.27\text{--}0.53 \mu\text{m s}^{-1}$) and $0.5 \mu\text{m s}^{-1}$ retrograde (range = $0.32\text{--}0.60 \mu\text{m s}^{-1}$), and maximum run velocities of $2.6 \mu\text{m s}^{-1}$ anterograde (range = $1.7\text{--}2.6 \mu\text{m s}^{-1}$) and $3.2 \mu\text{m s}^{-1}$ retrograde (range = $2.3\text{--}3.2 \mu\text{m s}^{-1}$) (Uchida and Brown, 2004; Uchida et al., 2009; Wang and Brown, 2001, 2010; Wang et al., 2000). In contrast, in the present study we measured average run velocities of $0.89 \mu\text{m s}^{-1}$ anterograde and $1.18 \mu\text{m s}^{-1}$ retrograde, and maximum sustained run velocities of $6.6 \mu\text{m s}^{-1}$ anterograde and $7.8 \mu\text{m s}^{-1}$ retrograde. Thus, on short time scales, neurofilament polymers move even faster than we previously appreciated, and at speeds comparable to membranous

organelles (Reis et al., 2012). What distinguishes neurofilament movement is its intermittent nature; the average velocities are much slower than those for membranous organelles on longer time scales because the rapid movements of neurofilaments are interrupted by frequent and sometimes prolonged pauses (Brown, 2000, 2003, 2014; Li et al., 2012).

4.2 | Implications for the Mechanism of Movement

Inspection of the filament trajectories also revealed considerable complexity to the kinetic behaviors of these polymers. While all filaments exhibited alternating runs and pauses, the direction and velocity of movement were variable. Many filaments appeared to have a preferred direction that was retained during intervening pauses, but often these filaments also exhibited frequent brief reversals, some as short as one or two time intervals ($\sim 30\text{--}60$ ms). In some cases, the filaments reversed repeatedly with little delay or directional preference as if shuttling to and fro. This behavior is reminiscent of a tug-of-war (Soppina, Rai, Ramaiya, Barak, & Mallik, 2009) and suggests that single filaments can be bound stably and simultaneously (at least over a period of minutes) to both kinesin and dynein motors. We are currently developing a motor-based computational model of neurofilament transport to test this hypothesis, and the data set described here forms the foundation for that study. Remarkably, the filaments also appeared to remain fully extended while reversing. We have noted the tendency for neurofilaments to move in a fully outstretched configuration previously, and we speculated that it may suggest that the motors form preferential associations with the ends of the filaments (Taylor et al., 2012). The fact that the filaments can remain outstretched even when reversing suggests that opposite ends of the same filament may recruit motors of opposing directionality. We plan to test this hypothesis experimentally in the near future, though we recognize that it is puzzling mechanistically because neurofilaments are nonpolar polymers so their two ends should be structurally equivalent.

4.3 | Filament Barcoding

An interesting feature of the kymographs was the striped appearance of some of the filaments, which we have termed “barcoding” (see Figure 3c). These stripes reflect non-uniformities in the fluorescence along the filaments that are not obvious in the raw movies because of their low signal-to-noise ratio, but are clear in the kymographs because the alignment of the linear intensity profiles has an effect similar to temporal averaging. A similar barcoding pattern has been observed in kymograph analyses of motor-dependent gliding of microtubules assembled in vitro from a mixture of fluorescently labeled and nonlabeled tubulin dimers (e.g., Alper, Tovar, & Howard, 2013). Thus, neurofilament barcoding could be caused by random variation in the incorporation of the GFP-NFM fusion protein along the length of the filaments. However, we have also noted that filaments within the same axon can vary in brightness, perhaps due to variation in the time of assembly relative to the temporal expression profile of the GFP-NFM fusion protein in these transiently transfected cells. Thus, the neurofilament barcoding

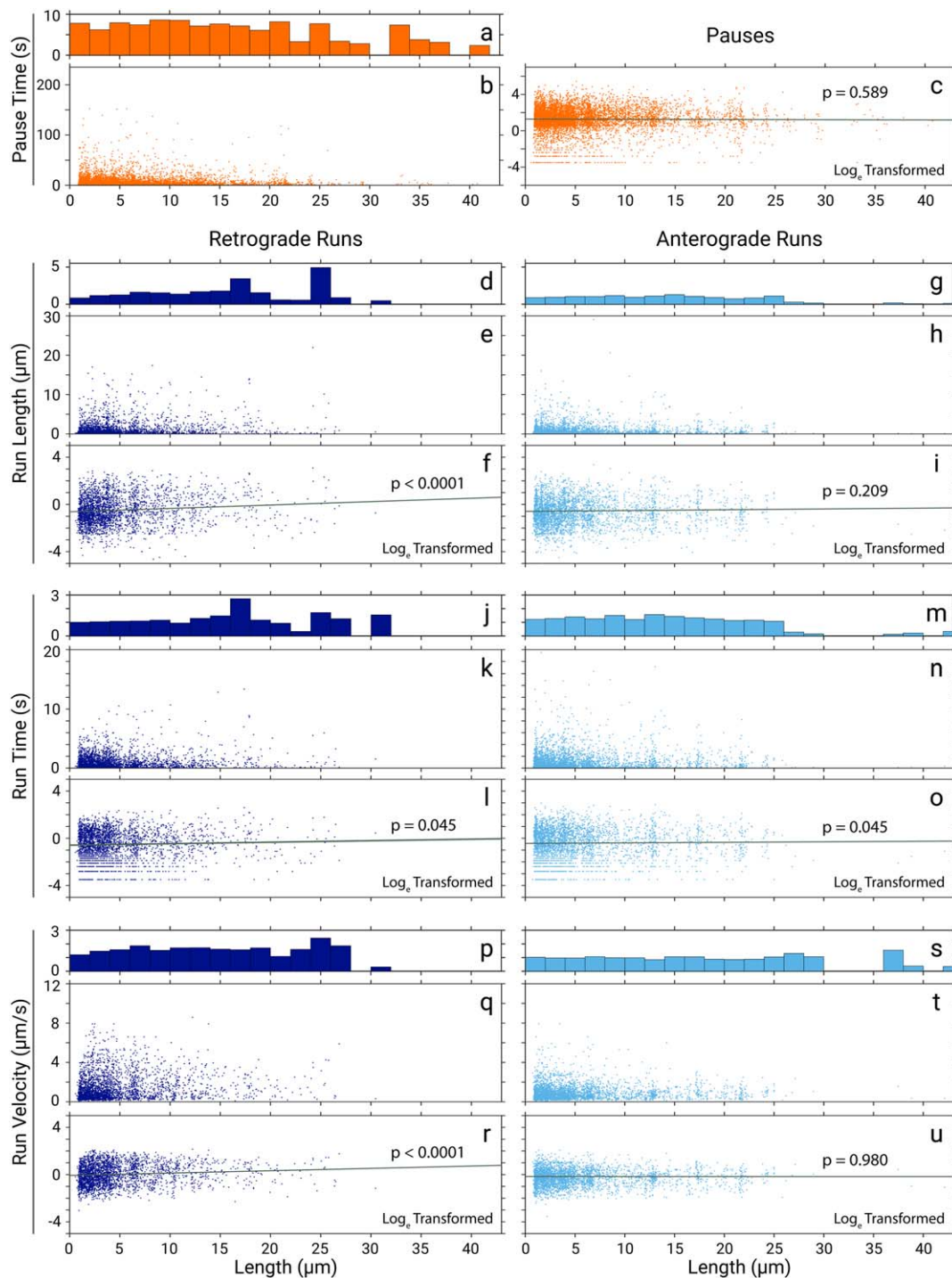


FIGURE 12 Dependence of the transport kinetics on filament length. We plotted the four kinetic parameters of filament movement (pause time, run length, run time, and run velocity) as a function of filament length, which ranged from 0.6 to 42.1 μm . Histograms of the average filament lengths with 2 μm bins are shown in (a, d, g, j, m, p, and s). Scatter plots of the raw data are shown in (b, e, h, k, n, q, and t). Scatter plots of the natural log-transformed raw data are shown in (c, f, i, l, o, r, and u). Each data point in the scatter plots represents the parameter value for a single run. The slopes represent the linear regression fit to the natural log-transformed data generated by a statistical analysis using a mixed effects model. The p values for the statistical tests are shown on the plots next to the regression lines. (a–c) The analysis revealed no relationship between pause time and filament length. (d–f), (p–r) The analysis revealed a statistically significant increase in retrograde run length and run velocity with increasing filament length. (g–i), (s–u) The analysis revealed no statistically significant change in anterograde run length and run velocity with increasing filament length. These differences in the length-dependence of the retrograde and anterograde run length and run velocity were statistically significant ($p = 0.001$ and $p = 0.0002$, respectively). (j–l), (m–o) The analysis revealed a statistically significant increase in run time with increasing filament length, but no significant difference between anterograde and retrograde runs in this respect ($p = 0.27$). Thus, the p value shown in panels (l and o) is the p value for main effect of filament length on anterograde and retrograde runs combined [Color figure can be viewed at wileyonlinelibrary.com]

could also reflect the severing and annealing dynamics of these polymers that we have reported previously (Colakoglu and Brown, 2009; Uchida, Colakoglu, Wang, Monsma, & Brown, 2013), with dark and light stripes arising due to annealing of short filaments containing different proportions of the GFP-NFM fusion protein. A similar mechanism could explain the discrete contiguous phosphorylated and nonphosphorylated domains we have observed previously along axonal neurofilaments, if we assume that phosphorylation is a marker of neurofilament age (Brown, 1998).

4.4 | Technical Considerations

Kinetic studies on the movement of intracellular cargoes depend on the unambiguous identification of runs and pauses. Because nothing is truly stationary at the molecular level, this requires distinguishing passive (Brownian) motion from active (motor-driven) motion. This was a challenge for the present study because of the pixelated and noisy nature of the kymographs. Our pause-smoothing/run-filtering computational algorithm is an automated solution to this problem, and our error analysis revealed good agreement between the processed and raw traces. Thus, we are confident that this algorithm was precise and that the filtered traces accurately reflect the motion recorded in the original kymographs. However, this method requires the selection of a noise threshold and a pause cut-off that must be identified empirically. A consequence of the pause cut-off requirement is that it introduces an artificial minimum pause duration. For our chosen threshold of $0.1 \mu\text{m s}^{-1}$, this minimum pause duration was 53 frames, or 1 pixel (160 nm) in 1.6 s. Thus, any slow creeping movements that fall below this threshold would not be considered a movement in our analysis.

The quality of the edge detection is a critical step in our analysis, and it is very sensitive to image noise. The Canny-Deriche algorithm worked well when the signal-to-noise ratio was high, creating strong edge suppression channels that isolated the neurofilament edges from other spurious edges, but at low signal-to-noise, the edge suppression was weaker and gaps or branches were often encountered in the neurofilament edges. While we did edit branch points, we chose to not fill gaps in order to avoid bias. To ensure that these gaps did not lead us to underestimate the run lengths or run and pause times, we rejected any movement or pause that was flanked by one or two gaps in the trace. In other words, runs and pauses had to be flanked by other runs and/or pauses. The result was a more reliable data set, but this came at a cost, which was the rejection of about 35% of the data. We do not believe that this compromised our analysis because there is no reason to expect any correlation between transport kinetics and the signal-to-noise ratio of the filaments.

A striking feature of neurofilament transport is that it is dominated by long pauses. For example, our experimental and computational analysis of the long-term pausing behavior of neurofilaments in cell culture and *in vivo* has suggested that the filaments spend $\geq 97\%$ of their time pausing, and much of that time in an off-track prolonged pausing state with average pause times on the order of an hour or more (Li et al., 2012; Monsma, Li, Fenn, Jung, & Brown, 2014; Trivedi et al., 2007). It is important to note that the present study did not capture this

prolonged pausing behavior because of the short time frame of our movies. Moreover, our method of analysis relied on the detection of filaments moving through gaps in the axonal neurofilament array. Filaments that remain paused and that overlapped with other filaments could not be tracked because they could not be resolved from their neighbors. Thus, while the filaments analyzed in this study spent an average of 83.2% of their time pausing and exhibited average pause times of about 9 s, this is an underestimate of their pausing behavior on longer time scales.

4.5 | The Distribution of Filament Lengths

It is interesting to note that the length distribution of the neurofilaments in our study was approximately exponential (i.e., approximately linear on a semi-log plot; see Figure 11). This suggests an underlying uniformity to the filament population and an underlying randomness to the mechanisms that determine filament length. Sept, Xu, Pollard, & McCammon (1999) have described a similar length distribution for actin filaments assembled *in vitro* and they showed that this can be explained by incorporating filament annealing and fragmentation into their model of actin assembly. Because axonal neurofilaments are also subject to severing and annealing (Colakoglu and Brown, 2009; Uchida et al., 2013), it is attractive to speculate that the exponential distribution of filament lengths in neurons reflects a similar mechanism.

4.6 | Dependence of the Transport Kinetics on Filament Length

Moving neurofilaments in cultured neurons can exceed $30 \mu\text{m}$ in length, which makes these polymers by far the longest cargo structures conveyed by axonal transport (Wang and Brown, 2001, 2010). Within axons, neurofilaments are packed densely together and bristle with a dense brush border of radially projecting side arms, which are comprised of the carboxy terminal domains of the neurofilament polypeptides (Hirokawa, 1982; Mukhopadhyay, Kumar, & Hoh, 2004; Schnapp and Reese, 1982). Thus, it is conceivable that these polymers might experience significant drag during their movement through axonal cytoplasm and that this might increase with increasing polymer length. However, we found no decrease in run velocity, run time or run length with increasing filament length for either anterograde and retrograde runs. Similar findings were reported by Roy et al. (2000) based on a comparison of average velocities of a more limited dataset of 20 filaments (Roy et al., 2000). In addition, our analysis revealed a statistically significant increase in run velocity, run time and run length with increasing filament length for retrograde runs. The explanation for this increase is presently unclear, but the lack of any decrease in these kinetic parameters with increasing length for either direction of movement does appear to indicate that either neurofilaments experience minimal drag during their transport along axons, or alternatively that longer neurofilaments compensate for any increase in drag by recruiting more active motors. Whether this extends to filaments longer than those analyzed here is not clear. Neurofilaments in cultured neurons have been reported to reach lengths as long as $186 \mu\text{m}$ (Brown, 1997),

and the one published estimate in vivo reported average neurofilament lengths of 118 μm (Burton and Wentz, 1992). It would be interesting to know if neurofilaments in excess of 100 μm can move at speeds comparable to those reported in the present study, but tracking such filaments is challenging because they are rarely encountered in cultured neurons and because their length exceeds the dimensions of our camera field of view.

ACKNOWLEDGMENTS

This work was supported by NIH grant R01 NS038526 to AB, by collaborative NSF grants IOS 1656784 to AB and NSF IOS 1656785 to PJ, and by the Neuroscience Research Institute at The Ohio State University. The purchase and use of the microscope was made possible by NIH Small Instrumentation Grant S10 OD010383 and NIH Center Core Grant P30 NS045758.

ORCID

J. Daniel Fenn  <http://orcid.org/0000-0002-4253-6159>

Peter Jung  <http://orcid.org/0000-0002-1100-9946>

Anthony Brown  <http://orcid.org/0000-0003-2295-2929>

REFERENCES

- Alper, J. D., Tovar, M., & Howard, J. (2013). Displacement-weighted velocity analysis of gliding assays reveals that Chlamydomonas axonemal dynein preferentially moves conspecific microtubules. *Biophysical Journal*, 104, 1989–1998.
- Baas, P. W., Deitch, J. S., Black, M. M., & Banker, G. A. (1988). Polarity orientation of microtubules in hippocampal neurons: Uniformity in the axon and nonuniformity in the dendrite. *Proceedings of the National Academy of Sciences of the United States of America*, 85, 8335–8339.
- Brown, A. (1997). Visualization of single neurofilaments by immunofluorescence microscopy of splayed axonal cytoskeletons. *Cell Motility & the Cytoskeleton*, 38, 133–145.
- Brown, A. (1998). Contiguous phosphorylated and non-phosphorylated domains along axonal neurofilaments. *Journal of Cell Science*, 111, 455–67.
- Brown, A. (2000). Slow axonal transport: Stop and go traffic in the axon. *Nature Reviews Molecular Cell Biology*, 1, 153–156.
- Brown, A. (2003). Axonal transport of membranous and nonmembranous cargoes: A unified perspective. *Journal of Cell Biology*, 160, 817–821.
- Brown, A. (2014). Slow axonal transport. In M. Caplan (Ed.), *Reference Module in Biomedical Sciences*. Elsevier.
- Brown, A. (2016). Axonal transport. In D. W. Pfaff & N. D. Volkow (Eds.), *Neuroscience in the 21st Century: From Basic to Clinical* (pp. 333–379). New York: Springer Publishing.
- Brown, A., Wang, L., & Jung, P. (2005). Stochastic simulation of neurofilament transport in axons: The “stop-and-go” hypothesis. *Molecular Biology of the Cell*, 16, 4243–4255.
- Burton, P. R., & Wentz, M. A. (1992). Neurofilaments are prominent in bullfrog olfactory axons but are rarely seen in those of the tiger salamander, *Ambystoma tigrinum*. *Journal of Comparative Neurology*, 317, 396–406.
- Chaphalkar, A. R., Jain, K., Gangan, M. S., & Athale, C. A. (2016). Automated multi-peak tracking kymography (AMTrak): A tool to quantify sub-cellular dynamics with sub-pixel accuracy. *PLoS One*, 11, e0167620.
- Colakoglu, G., & Brown, A. (2009). Intermediate filaments exchange subunits along their length and elongate by end-to-end annealing. *Journal of Cell Biology*, 185, 769–777.
- Craciun, G., Brown, A., & Friedman, A. (2005). A dynamical system model of neurofilament transport in axons. *Journal of Theoretical Biology*, 237, 316–322.
- Deriche, R. (1987). Using Canny's criteria to derive a recursively implemented optimal edge detector. *International Journal of Computer Vision*, 1, 167–187.
- Efimov, A., Schiefermeier, N., Grigoriev, I., Ohi, R., Brown, M. C., Turner, C. E., ... Kaverina, I. (2008). Paxillin-dependent stimulation of microtubule catastrophes at focal adhesion sites. *Journal of Cell Science*, 121, 196–204.
- Francis, F., Roy, S., Brady, S. T., & Black, M. M. (2005). Transport of neurofilaments in growing axons requires microtubules but not actin filaments. *Journal of Neuroscience Research*, 79, 442–450.
- Gouveia, S. M., & Akhmanova, A. (2010). Cell and molecular biology of microtubule plus end tracking proteins: End binding proteins and their partners. *International Review of Cell and Molecular Biology*, 285, 1–74.
- He, Y., Francis, F., Myers, K. A., Yu, W., Black, M. M., & Baas, P. W. (2005). Role of cytoplasmic dynein in the axonal transport of microtubules and neurofilaments. *Journal of Cell Biology*, 168, 697–703.
- Heidemann, S. R., Landers, J. M., & Hamborg, M. A. (1981). Polarity orientation of axonal microtubules. *Journal of Cell Biology*, 91, 661–665.
- Helfand, B. T., Loomis, P., Yoon, M., & Goldman, R. D. (2003). Rapid transport of neural intermediate filament protein. *Journal of Cell Science*, 116, 2345–2359.
- Hirokawa N. (1982). Cross-linker system between neurofilaments, microtubules and membranous organelles in frog axons revealed by quick freeze deep etching method. *Journal of Cell Biology*, 94, 129–142.
- Hoffman, P. N. (1995). The synthesis, axonal transport, and phosphorylation of neurofilaments determine axonal caliber in myelinated nerve fibers. *The Neuroscientist*, 1, 76–83.
- Hoffman, P. N., & Lasek, R. J. (1975). The slow component of axonal transport: Identification of major structural polypeptides of the axon and their generality among mammalian neurons. *Journal of Cell Biology*, 66, 351–366.
- Jung, P., & Brown, A. (2009). Modeling the slowing of neurofilament transport along the mouse sciatic nerve. *Physical Biology*, 6, 046002.
- Kaech, S., & Banker, G. (2006). Culturing hippocampal neurons. *Nature Protocol*, 1, 2406–2415.
- Lasek, R. J., Garner, J. A., & Brady, S. T. (1984). Axonal transport of the cytoplasmic matrix. *Journal of Cell Biology*, 99, 212s–215s.
- Lasek, R. J., Paggi, P., & Katz, M. J. (1993). The maximum rate of neurofilament transport in axons: A view of molecular transport mechanisms continuously engaged. *Brain Research*, 616, 58–64.
- Li, Y., Brown, A., Jung, P. (2014). Deciphering the axonal transport kinetics of neurofilaments using the fluorescence photoactivation pulse-escape method. *Physical Biology*, 11, 026001.
- Li, Y., Jung, P., & Brown, A. (2012). Axonal transport of neurofilaments: a single population of intermittently moving polymers. *Journal of Neuroscience*, 32, 746–758.
- Monsma, P. C., Li, Y., Fenn, J. D., Jung, P., & Brown, A. (2014). Local regulation of neurofilament transport by myelinating cells. *Journal of Neuroscience*, 34, 2979–2988.

- Mukhopadhyay, R., Kumar, S., & Hoh, J. H. (2004). Molecular mechanisms for organizing the neuronal cytoskeleton. *Bioessays*, *26*, 1017–1025.
- Prahlad, V., Helfand, B. T., Langford, G. M., Vale, R. D., & Goldman, R. D. (2000). Fast transport of neurofilament protein along microtubules in squid axoplasm. *Journal of Cell Science*, *113*, 3939–3946.
- Reis, G. F., Yang, G., Szpankowski, L., Weaver, C., Shah, S. B., Robinson, J. T., ... Goldstein, L. S. (2012). Molecular motor function in axonal transport in vivo probed by genetic and computational analysis in *Drosophila*. *Molecular Biology of the Cell*, *23*, 1700–1714.
- Roy, S., Coffee, P., Smith, G., Liem, R. K. H., Brady, S. T., & Black, M. M. (2000). Neurofilaments are transported rapidly but intermittently in axons: Implications for slow axonal transport. *Journal of Neuroscience*, *20*, 6849–6861.
- Schindelin, J., Arganda-Carreras, I., Frise, E., Kaynig, V., Longair, M., Pietzsch, T., ... Schmid, B. (2012). Fiji: An open-source platform for biological-image analysis. *Nature Methods*, *9*, 676–682.
- Schnapp, B. J. & Reese, T. S. (1982). Cytoplasmic structure in rapid frozen axons. *Journal of Cell Biology*, *94*, 667–679.
- Schneider, C. A., Rasband, W. S., & Eliceiri, K. W. (2012). NIH Image to ImageJ: 25 years of image analysis. *Nature Methods*, *9*, 671–675.
- Seitz, A., & Surrey, T. (2006). Processive movement of single kinesins on crowded microtubules visualized using quantum dots. *EMBO Journal*, *25*, 267–77.
- Sept, D., Xu, J., Pollard, T. D., & McCammon, J. A. (1999). Annealing accounts for the length of actin filaments formed by spontaneous polymerization. *Biophysical Journal*, *77*, 2911–2919.
- Shah, J. V., Flanagan, L. A., Janmey, P. A., & Leterrier, J.-F. (2000). Bidirectional translocation of neurofilaments along microtubules mediated in part by dynein/dynactin. *Molecular Biology of the Cell*, *11*, 3495–3508.
- Soppina, V., Rai, A. K., Ramaia, A. J., Barak, P., & Mallik, R. (2009). Tug-of-war between dissimilar teams of microtubule motors regulates transport and fission of endosomes. *Proceedings of the National Academy of Science of the United States of America*, *106*, 19381–19386.
- Stepanova, T., Slemmer, J., Hoogenraad, C. C., Lansbergen, G., Dortland, B. D., Zeeuw, C. I., ... Galjart, N. (2003). Visualization of microtubule growth in cultured neurons via the use of EB3-GFP (end-binding protein 3-green fluorescent protein). *Journal of Neuroscience*, *23*, 2655–2664.
- Taylor, N. J., Wang, L., & Brown, A. (2012). Neurofilaments are flexible polymers that often fold and unfold but they move in a fully extended configuration. *Cytoskeleton (Hoboken)*, *69*, 535–544.
- Trivedi, N., Jung, P., & Brown, A. (2007). Neurofilaments switch between distinct mobile and stationary states during their transport along axons. *Journal of Neuroscience*, *27*, 507–516.
- Uchida, A., Alami, N. H., & Brown, A. (2009). Tight functional coupling of kinesin-1A and dynein motors in the bidirectional transport of neurofilaments. *Molecular Biology of the Cell*, *20*, 4997–5006.
- Uchida, A., & Brown, A. (2004). Arrival, reversal and departure of neurofilaments at the tips of growing axons. *Molecular Biology of the Cell*, *15*, 4215–4225.
- Uchida, A., Colakoglu, G., Wang, L., Monsma, P. C., & Brown, A. (2013). Severing and end-to-end annealing of neurofilaments in neurons. *Proceedings of the National Academy of Science of the United States of America*, *110*, E2696–E705.
- Uchida, A., Monsma, P. C., Fenn, J. D., & Brown, A. (2016). Live-cell imaging of neurofilament transport in cultured neurons. *Methods in Cell Biology*, *131*, 21–90.
- Wagner, O. I., Ascano, J., Tokito, M., Leterrier, J. F., Janmey, P. A., & Holzbaur, E. L. (2004). The interaction of neurofilaments with the microtubule motor cytoplasmic dynein. *Molecular Biology of the Cell*, *15*, 5092–5100.
- Wang, L., & Brown, A. (2001). Rapid intermittent movement of axonal neurofilaments observed by fluorescence photobleaching. *Molecular Biology of the Cell*, *12*, 3257–3267.
- Wang, L., & Brown, A. (2010). A hereditary spastic paraplegia mutation in kinesin-1A/KIF5A disrupts neurofilament transport. *Molecular Neurodegeneration*, *5*, 52.
- Wang, L., Ho, C.-L., Sun, D., Liem, R. K. H., & Brown, A. (2000). Rapid movement of axonal neurofilaments interrupted by prolonged pauses. *Nature Cell Biology*, *2*, 137–141.
- Waterman-Storer, C. M., Desai, A., Bulinski, J. C., & Salmon, E. D. (1998). Fluorescent speckle microscopy, a method to visualize the dynamics of protein assemblies in living cells. *Current Biology*, *8*, 1227–1230.
- Yan, Y., & Brown, A. (2005). Neurofilament polymer transport in axons. *Journal of Neuroscience*, *25*, 7014–7021.
- Yan, Y., Jensen, K., & Brown, A. (2007). The polypeptide composition of moving and stationary neurofilaments in cultured sympathetic neurons. *Cell Motility & Cytoskeleton*, *64*, 299–309.
- Yau, K. W., Schatzle, P., Tortosa, E., Pages, S., Holtmaat, A., Kapitein, L. C., & Hoogenraad, C. C. (2016). Dendrites in vitro and in vivo contain microtubules of opposite polarity and axon formation correlates with uniform plus-end-out microtubule orientation. *Journal of Neuroscience*, *36*, 1071–1085.
- Zhang, K., Osakada, Y., Xie, W., & Cui, B. (2011). Automated image analysis for tracking cargo transport in axons. *Microscopy Research & Techniques*, *74*, 605–613.

SUPPORTING INFORMATION

Additional Supporting Information may be found online in the supporting information tab for this article.

How to cite this article: Fenn JD, Johnson CM, Peng J, Jung P, Brown A. Kymograph analysis with high temporal resolution reveals new features of neurofilament transport kinetics. *Cytoskeleton*. 2018;75:22–41. <https://doi.org/10.1002/cm.21411>